III. R & D RELATED TO A FUTURE RARE ISOTOPE ACCELERATOR FACILITY

OVERVIEW

The Rare Isotope Accelerator (RIA), a next-generation facility for basic research in nuclear physics, continues to be a high priority for construction in the United States by the Department of Energy Office of Science. In late 2003 RIA was ranked a very high priority in the Office of Science 20-year plan. The CD-0 milestone for RIA was expected to be passed in early 2004, and work on the RIA Conceptual Design Report could begin during FY2005. To prepare for RIA design and construction it is essential to continue a vigorous R&D program for RIA. This section is a progress report on the RIA R&D efforts at Argonne during 2003.

The RIA R&D topics addressed at Argonne during the year 2003 fall in two main sub-sections of this chapter: (A) Heavy Ion Linac Technology: Beam Dynamics, Room Temperature Structures, and Superconducting RF, and (B) Rare Isotope Production and Separation.

We continued to develop and improve the baseline design for the RIA proposal. Highlights of developments during 2003 include:

- Successful operation of several prototype superconducting drift-tube resonator structures at peak surface fields of 30 MV/m or higher.

- Development of an alternative RIA Driver Linac option based on a 345-MHz triple-spoke resonator concept.

- Continued improvement of the Driver Linac beam dynamics to quantify the effects of misalignment and RF setting errors, and the development of algorithms for the implementation of steering corrections.

- Construction and testing of cold models of RFQ's for both the Driver Linac and RIB Post Accelerators.

- Completion of the design of a novel adjustable-thickness, liquid-lithium target for use with heavy ion beams up to 4 kW for in-flight fragmentation at the NSCL A1900 fragment separator.

- Demonstration of a high power windowless liquid lithium target in operation with a 20-kW electron beam to simulate the total power deposited by a 200-kW uranium beam.

- Completion and characterization of a full-scale RIA prototype fast gas catcher.

- Extension of fragment separator simulations to include predictions of secondary beam impurities due to secondary reactions in the degrader foils.

A. HEAVY-ION LINAC TECHNOLOGY: BEAM DYNAMICS, ROOM TEMPERATURE STRUCTURES, AND SUPERCONDUCTING RF

a.1.   Beam Loss Studies in High-Intensity Heavy-Ion Linacs (P. N. Ostroumov, V. N. Aseev, and B. Mustapha)

To produce sufficient intensities of secondary beams the RIA driver linac will provide 400-kW primary beams of any ion from hydrogen to uranium. Due to the high-intensity of the primary beams, the beam losses must be minimized to avoid radioactivation of the accelerator equipment.   To keep the power deposited by the particles lost on the accelerator structures below 1 Watt/m, the relative beam losses per unit length should be less than 10^{-5}, especially along the high-energy section of the linac. A new beam dynamics simulation code TRACK was developed and used for beam loss studies in the RIA driver linac. In the TRACK code, ions are tracked through the three-dimensional electromagnetic fields of every element of the linac starting from the ECR (Electron Cyclotron Resonance) ion source to the production target. The simulation starts with a multi-component DC ion beam extracted from the ECR. The space charge forces are included in the simulations. They are especially important in the front end of the driver linac. Beam losses are studied by tracking a large number of particles (up to 10^6) through the whole linac considering all sources of error such as element misalignments, RF field errors and stripper thickness fluctuations.   For each configuration of the linac, multiple sets of error values were randomly generated and used in the calculations.   The results are then combined to calculate important beam parameters, estimate beam losses and characterize the corresponding linac configuration.   To track large numbers of particles for a comprehensive number of error sets (up to 500), the code TRACK was parallelized and run on the Jazz computer cluster at ANL.

In accelerators one can distinguish controlled and uncontrolled beam losses. The controlled losses are the particles collected by intercepting any beam halo with specially designed collimators located at designated areas along the accelerator. All other losses anywhere along the linac are considered as uncontrolled losses. The main source of beam losses is the formation of beam halo either in longitudinal or transverse phase spaces. In the simulation, a particle is considered lost if it is outside the physical transverse aperture of the linac. Massive parallel-computer simulations were performed for two options of the SC driver linac in order to

investigate possible beam losses and determine the exact location of these eventual losses. The first option is the baseline design of the driver linac based on elliptical cell cavities (ECL) and the second option of the driver linac is based on triple-spoke resonators (TSL) in the high-β section of the linac.

The results of end-to-end beam dynamics simulations of two options for the RIA driver linac are presented in Table III-1 and Fig. III-1. Both the baseline and triple-spoke designs of the accelerator were simulated using 200 sets of errors for each error combination shown in Table III-1. Figure III-1 shows phase space plots at the exit of the accelerator for the different error combinations. From these plots we notice that while the transverse size of the beam stays unchanged for the triple-spoke design it is increasing for the baseline design signaling a growth in the transverse emittance. The transverse emittance growth in the ECL design is following the growing longitudinal emittance.   This may be due to a coupling of the transverse and longitudinal motion for particles near the separatrix in the longitudinal phase space. Some of these particles may lose their stability and eventually be lost. Table III-1 shows the fraction of beam lost in the high-β sections of the linac for the different error combinations and both accelerator designs. The values in Table III-1 are the average over the 200 sets of errors for each combination. Beam losses are observed in the high-β section for the baseline design whereas no losses are observed for the triple-spoke design. The losses seem to increase with both the RF errors and the fluctuation in the stripper thickness. Keeping the stripper thickness fluctuation at 5% FWHM (combinations 3 and 5) and increasing the RF errors from (0.5%, 0.5°) to (0.7%, 0.7°) leads to more losses in the high energy section than increasing the thickness fluctuation from 5% FWHM to 10% FWHM (combinations 3 and 4) while keeping the RF errors at (0.5%, 0.5°). This signals a more important beam halo formation for RF errors compared to stripper thickness fluctuation. Therefore RF errors should be kept as small as possible. The error on the thickness fluctuation should also be limited to about 5% FWHM or less in the baseline design. The losses in the ECL are extremely sensitive to the longitudinal tuning of the linac in terms of phase setting to produce the lowest possible effective emittance at the

location of the strippers. The triple-spoke design is more tolerant of errors without producing any uncontrolled beam losses in wide range of RF errors, thickness fluctuations of the strippers and overall longitudinal tuning of the linac.

Table III-1. Uncontrolled beam losses for the error combinations and both the baseline and triple spoke designs of the driver linac.

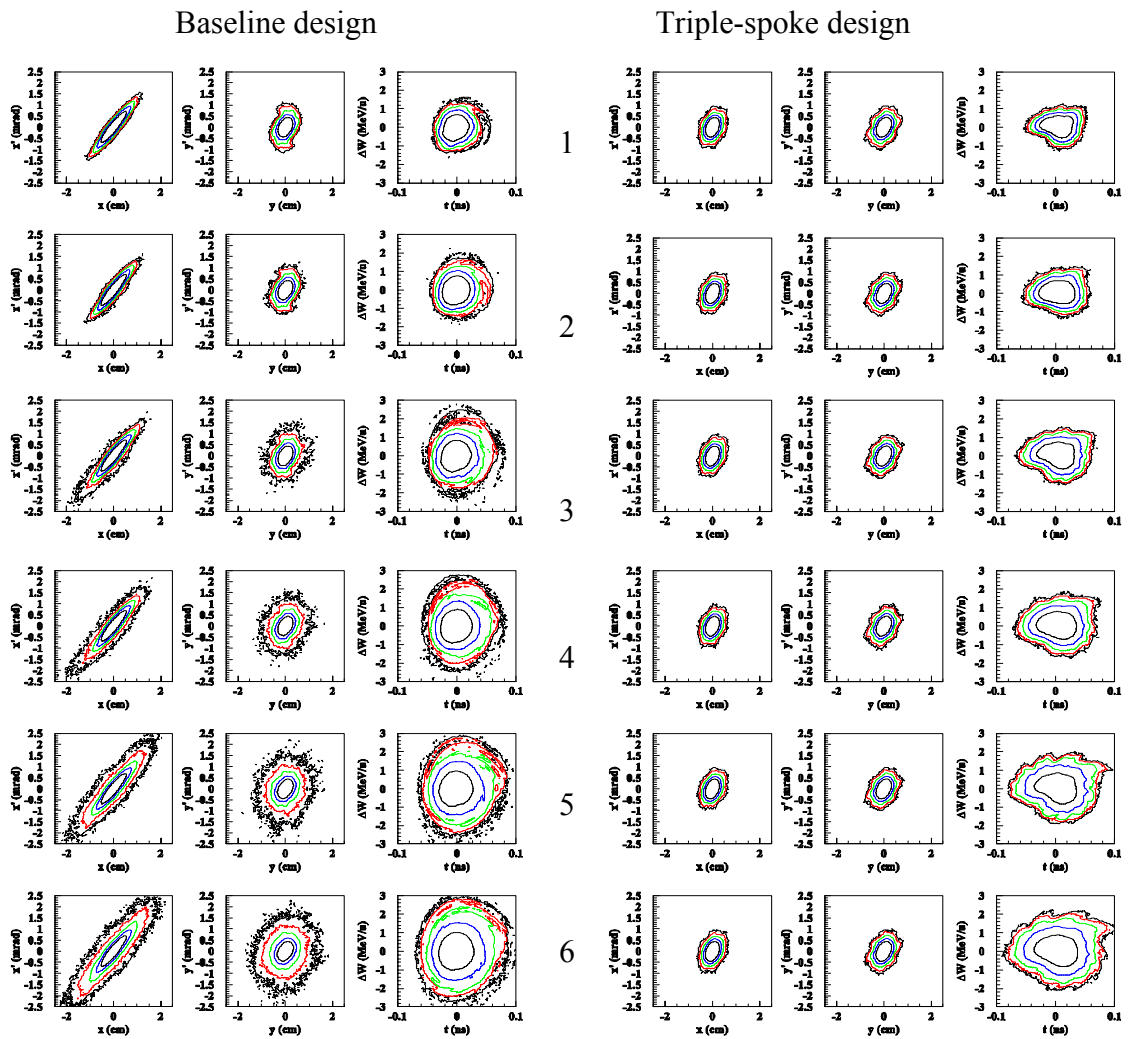| Combination	RF errors (field, phase)	Thickness fluctuation	Losses Baseline	Losses Triple spoke
1	0.3%, 0.3°	5% (FWHM)	3.0×10^{-8}	0.
2	0.3%, 0.3°	10% (FWHM)	8.2×10^{-7}	0.
3	0.5%, 0.5°	5% (FWHM)	5.5×10^{-5}	0.
4	0.5%, 0.5°	10% (FWHM)	2.7×10^{-4}	0.
5	0.7%, 0.7°	5% (FWHM)	1.4×10^{-3}	0.
6	0.7%, 0.7°	10% (FWHM)	2.6×10^{-3}	0.

Fig. III-1. Phase space plots for the different error combinations of Table III-1 (see numbers in the middle column). The logarithmic density isolines are represented by different color.

a.2   Stripper Parameterization For Heavy-Ion Beam Dynamics Simulations
(B. Mustapha, P. N. Ostroumov, and J. A. Nolen)

When accelerating heavy ions, stripping the beam increases the charge state and makes the acceleration more effective to reach higher beam energies. Scattering off the atoms of a stripper foil, a given ion not only loses electrons but also loses energy and deviates from its original direction. Therefore, the stripping process changes the properties of the beam depending on its energy and the stripper thickness. Strippers are usually thin and chosen to keep acceptable beam properties and minimal losses by inelastic interactions. Knowing the distributions of the beam energy loss and angle scattering after a stripper is important for beam dynamics simulations. For calculations where ions are tracked individually through the entire accelerator it is also important to be able to calculate or generate the energy loss and scattering angle ion by ion.

Full Monte-Carlo calculations of ions energy-loss and angle scattering like the code SRIM[1] are reliable but usually slow and not easy to couple to a beam dynamics code like TRACK.[2]   The calculation time is proportional to the stripper thickness because an incident ion is tracked through the different atomic layers of the stripper foil. In the case of the second stripper of the proposed RIA driver linac, the SRIM calculation time is comparable to tracking the same number of ions through the entire linac which would double the beam dynamics calculation time. As an alternative, we opt for the parameterization of the correlated energy-loss and angular distributions calculated with the code SRIM for a given beam-stripper combination.

Figure III-2 illustrates the basis of the parameterization method. The figure corresponds to the case of the second stripper in the RIA driver linac for which we used a 15-mg/cm^2 carbon foil. The beam is an 85-MeV/u ^{238}U beam. SRIM calculations were performed for 1 million incident ions. Studying the energy and angle distributions and their correlations, we noticed that for a selected small interval in angle squared θ^2, the corresponding energy distribution has a Gaussian-like shape, see Fig. III-3c. The θ^2 distribution itself is a portion of a decaying exponential, see Fig. III-3b. We noticed also that for different intervals in θ^2, the slope of the exponential as well as the center and width of the corresponding energy Gaussian are different. The linear correlation between E and θ^2 indicates that the center of the energy Gaussian should be a linear function of θ^2.
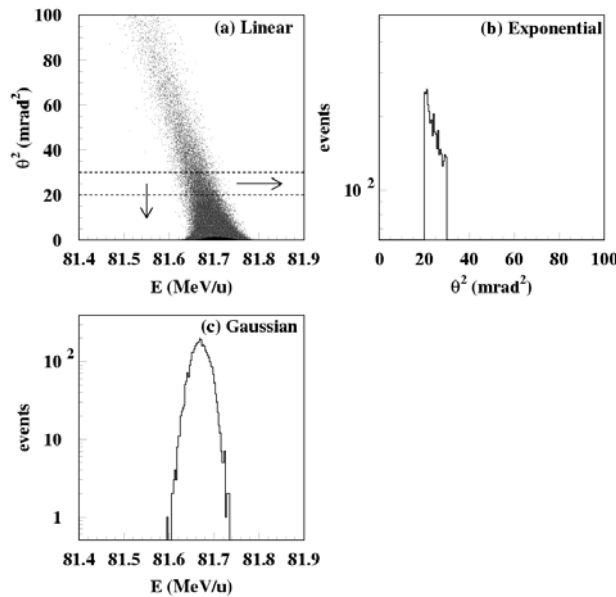

Fig. III-2. Basis of the parameterization. (a) shows the linear correlation between the energy and angle squared. (b) is the projection on angle squared of the selected small interval on (a) showing an exponential distribution, (c) is the projection on energy of the same angle interval suggesting a Gaussian distribution for every small angle interval.

The code SRIM assumes that the thickness of the stripper is well defined. Therefore a simple parameterization of SRIM results does not consider any fluctuation in the stripper thickness. We know that depending on the homogeneity of the material and its manufacturing there could be some fluctuations in the thickness of a stripper foil. This means that ions of the beam see different stripper thickness which usually results in an additional dispersion in the beam energy that exceeds the one coming from the statistical fluctuations in the energy loss. SRIM calculations performed for a ±5% and ±10% deviations from the nominal thickness of the second stripper showed that a 5% thickness fluctuation would increase the beam energy dispersion by a factor of ~3 and a 10% fluctuation would increase it by a factor of ~5. In order to consider the effect of thickness fluctuation in our parameterization we repeated the procedure described above to the case of the ±5% and ±10% thickness deviations.

Experimental measurements[3] suggested the thickness distribution of a stripper foil could be represented by a Gaussian distribution. The center of which is the average thickness and its FWHM (full width at half maximum) measures the thickness fluctuation. In order to check how well the thickness fluctuation is represented in the parameterization we have tested it against experimental data. Recent measurements at the AGS-BNL where a carbon foil is used to strip a 100 MeV/u Au beam from charge state 31^+ to 77^+ showed that even within the beam size these fluctuations could reach 10% FWHM.[3] The measurement was performed using a 4 MeV proton beam on a 0.005 inch carbon foil. Figure III-3 shows the comparison of the energy spectrum of the protons between the data, SRIM calculation (0% thickness fluctuation) and the parameterization of SRIM results considering a 10% FWHM thickness fluctuation. We clearly notice that the experimental data are very well reproduced by the parameterization with a 10% FWHM thickness fluctuation.

---

[1] SRIM/TRIM: http://www.srim.org.

[2] P. N. Ostroumov and V. N. Aseev, TRACK- a code for Beam Dynamics Simulations in SC Linac with 3D Electric and Magnetic Fields. ANL Technical Report, 2003.
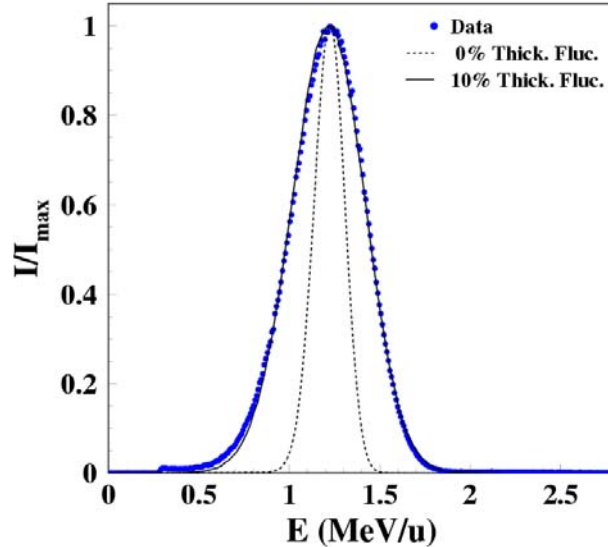
[3] P. Thieberger, private communication.

Fig. III-3. Effect of thickness fluctuation: Comparison of the experimental data with SRIM calculation (0% thickness fluctuation) and the parameterization using 10% FWHM thickness fluctuation. The data were measured using a 4 MeV proton beam on a 0.005 inch carbon foil.[3]

a.3.   Design of the RIA Driver Linac Front End (P. N. Ostroumov, V. N. Aseev,
A. A. Kolomiets, R. C. Pardo, and N. E. Vinogradov)

The Front End of the Driver Linac must form high-quality dual charge state heavy-ion beams with total transverse normalized emittance ~0.6 π mm-mrad and longitudinal emittance ~2 π kev/u-nsec at 99.5% level of the total beam intensity. The Front End consists of an ECR ion source located on a high-voltage platform, low energy beam transport (LEBT), RFQ and medium energy beam transport (MEBT). The LEBT includes two main sections: 1) an achromatic bending system for charge-to-mass analysis that can select one- or two-charge-state heavy ion beams; 2) a straight section with the Multi-Harmonic Buncher (MHB) that forms the longitudinal emittance and provides beam matching to the following RFQ (see Figure III-4). The achromatic system consists of two 60° bending magnets, six electrostatic quadruple lenses and a solenoid. A high dispersion area is formed by the first magnet where the required one- or two-charge state beam can be defined and transported to the RFQ. The baseline design of the RIA driver linac calls for a 400 kW uranium beam that requires a total of ~8 pµA in charge states 28^+ and 29^+. To compensate the linear component of the space charge forces a solenoid magnet between the ECR and bending magnet is used. It was found that changing solenoid position and field level provides required beam matching to the location of the horizontal slits for

wide range of extracted beam currents. The straight section of the LEBT includes a MHB, a velocity equalizer (VE), electrostatic quadruples and SC solenoid. All elements of this section except the solenoid are placed on a high-voltage platform. The distance between MHB and VE is determined by the need to separate the two charge states into adjacent RF buckets of the RFQ and is equal to *1.507 m* for the heaviest ions $^{238}U^{29+}$ and $^{238}U^{28+}$ at $V_0 = 100\ kV$. The electrostatic quadruples are used for beam focusing in this section of the LEBT and form a round beam waist both in the MHB and in the VE.

The beam dynamics simulations in the Front End were carried out using the code TRACK. Figure III-5 shows the obtained two-charge state uranium beam envelopes along the LEBT, RFQ and MEBT. Transverse and longitudinal phase space plots are shown at the end of the MEBT. Beam parameters are matched to the acceptance of the SC linac. These simulations were performed for $4 \cdot 10^4$ particles without space charge and higher-order corrections along the LEBT. Rms emittance growth in this simulations is 11%. We plan to continue our studies of beam optics in order to minimize emittance growth and halo formation in the Front End.
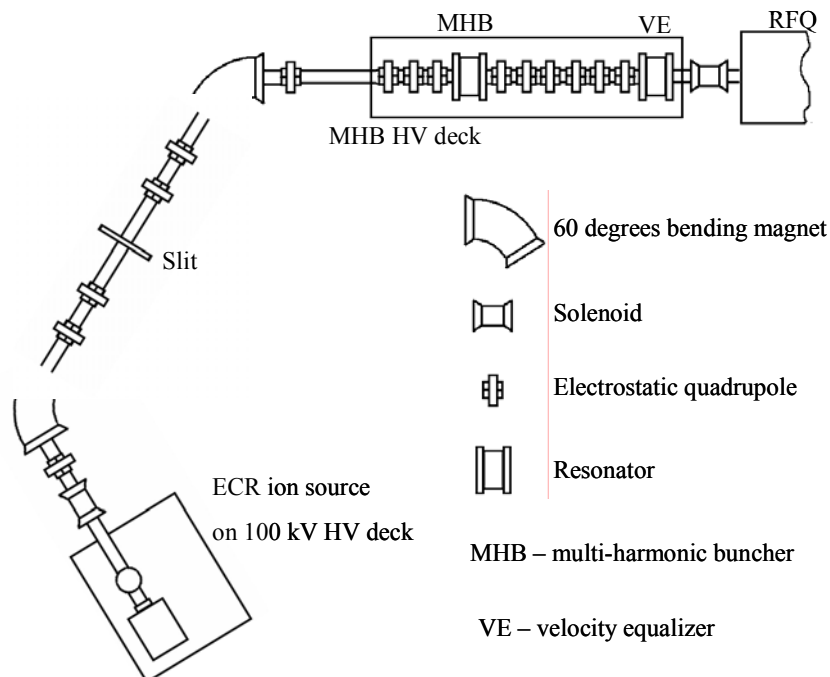

MHB   VE   RFQ

MHB HV deck

Slit

60 degrees bending magnet

Solenoid

Electrostatic quadrupole

Resonator

MHB – multi-harmonic buncher

VE – velocity equalizer

ECR ion source
on 100 kV HV deck

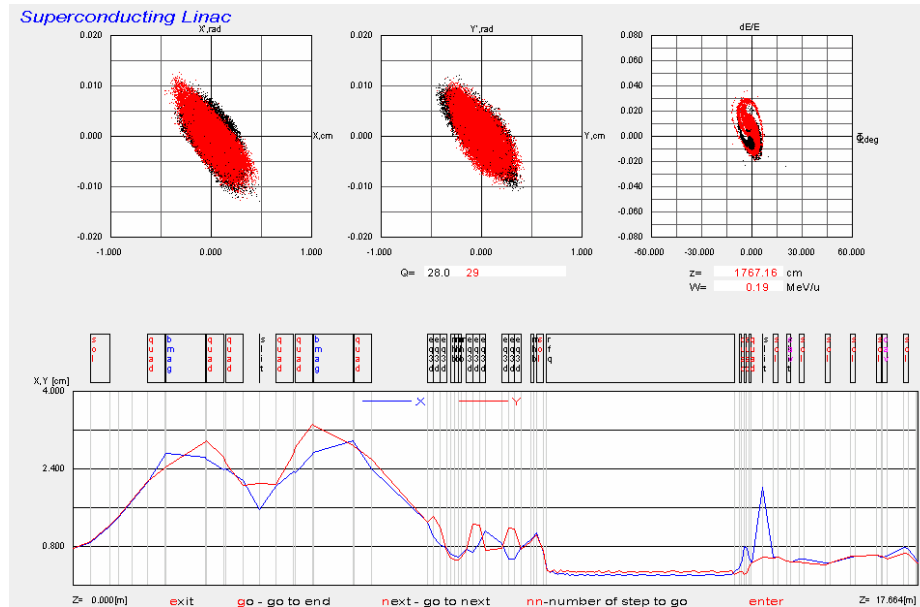*Fig. III-4. Basic layout of the Driver Linac Front End.*

Fig. III-5. Two charge state uranium beam envelopes along the LEBT-RFQ-MEBT.

a.4.   **57.5 MHz RFQ Cold Model** (P. N. Ostroumov and N. E. Vinogradov)

The RIA Driver includes a normal-conducting Radio Frequency Quadrupole (RFQ) accelerator operating in continuous wave mode. The 1:1 aluminum cold model of the 57.5 MHz RFQ segment has been designed and built. The structure with opened end caps is shown in the Fig. III-6. The dimensions of the model were defined using Micro Wave Studio (MWS) electrodynamics code.   For this purpose the Pro-Engineering drawings have been imported into the MWS computer code.   Additional simulations were carried out by the SLAC group using parallel finite-element eigensolver Omega3P with adaptive mesh refinement. Table III-2 shows the comparison between calculations and experimental measurements.   The MWS code reproduces the resonator frequency spectrum reasonably well and provides 1.5% accuracy for the lowest operating mode. However, the Omega3P code predicts the operating frequency much better. The

quality factor of the aluminum model was measured as 77% of the MWS calculated value.

As the next step of computer simulations, the transverse size of the cavity has been iteratively changed to establish the resonator dimensions to obtain exact resonant frequency which is 57.5 MHz. These calculations have been done using both MWS and High-Frequency Structure Simulator (HFSS) codes with the geometry exported from Pro-Engineering drawings. The results are shown in the Fig. III-7. As is seen from the graph, the results obtained from different codes are in a good agreement. The transverse size 19.2″ of the octagonal cross-section has been chosen for the construction of full power prototype. Currently the prototype is being fabricated.

---

[1]K. Kwok, SLAC
[2]G. Waldschmidt, ANL/APS.

Table III-2. Electrodynamics parameters of the aluminum pmodel.

Parameter	MWS	Omega3P	Experiment
Frequency of the 1st mode	55.276	54.603	54.469
Frequency of the 2nd mode	93.658		93.103
Frequency of the 3d mode	94.321		93.704
Frequency of the 4th mode	194.699		195.937
Frequency of the 5th mode	232.809		248.725
Quality factor of the 1st mode	6500	5829	4984

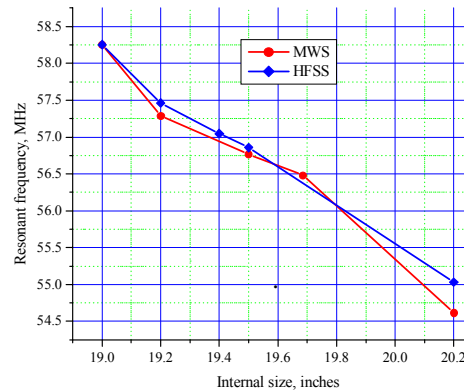Fig. III-6. *Aluminum cold model of the 57.5-MHz RFQ segment with opened end caps.*

Fig. III-7. *Resonant frequency of the segment as a function of a transverse dimension of the resonator.*

a.5.   Development of the 2Q-LEBT Prototype (N.E. Vinogradov, R. Scott, P. N. Ostroumov, and R. C. Pardo)

The concept of simultaneous acceleration of dual charge state heavy-ion beams in the RIA Driver Linac was developed earlier. For experimental confirmation of this concept as well as for testing of other components of the driver front end, it was decided to build a prototype injector which includes an ECR ion source, a LEBT and one-segment of the prototype RFQ. The project, called 2Q-LEBT Facility, is being developed at the high bay area of the Physics Division Dynamitron.

Currently, the 2Q-LEBT Facility consists of BEI-100 ECR ion source, which was designed and built by Berkeley Ion Equipment Corporation. The rf transmitters, high-voltage power supplies, turbo pumps and other related equipment were received with the source. BEI-100 is the all-permanent-magnet source utilizing NdFeB magnetic material, grade N45H, and has the highest magnetic field strengths for an ECR ion source of this type ever built. Figure III-8 shows an example of axial field profile measured experimentally and calculated using Electro Magnetic Studio code. The radial field provided by sextupole magnet achieves maximum strength of 11 kG at the plasma chamber surface. The source operates with two-frequency plasma heating of 12.75 and 14.5 GHz. We made appreciable modifications of the ECR components to increase the beam production performance. For example, one of the critical system of the ECR, the device for the injection of rf power and operational gas was damaged during the transportation (see Fig. III-9b). The design of the injection device was improved (see Fig. III-9a) and fabricated using the high-temperature vacuum brazing technique. The assembling of the source has been basically completed and the beam production is expected in the beginning of June 2004.

At the next steps of the 2Q-LEBT Project, the ion source will be installed on 100-kV high-voltage platform. Achromatic bending system, beam transport system including multi-harmonic buncher (MHB) and electrostatic quadrupoles for 3D matching of two-charge-state beam to following RFQ, and 57.5-MHz RFQ segment will be constructed. The achromatic bending system consists of two 60° bending magnets. The design of the bending magnets and MHB resonators is now in progress. The 57.5-MHz RFQ segment is being fabricated using high-temperature brazing in hydrogen atmosphere. Full tests of 2Q-beam capability are planned during FY2005.
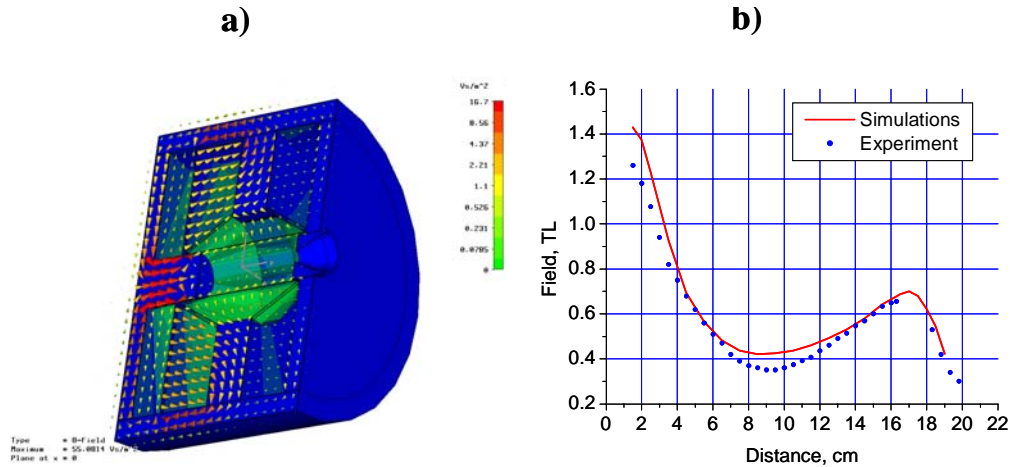
a)   **b)**

Fig. III-8. ECR plasma chamber in the EM Studio (a) and measured and simulated axial magnetic field profiles (b).

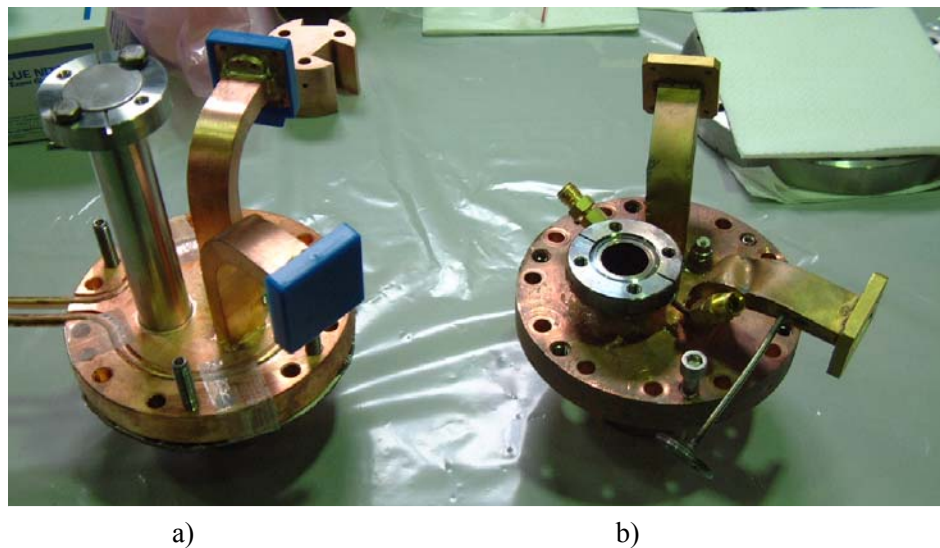a)   b)

Fig. III-9. The ECR damaged original (b) and modified new (a) injection devices.

a.6.   Multiple-Charge-State Beam Steering in High-Intensity Heavy-Ion Linacs
(E. S. Lessner and P. N. Ostroumov)

An algorithm suitable for correction to steering of multiple-charge-state beams in heavy-ion linacs operating at high currents was developed. It follows a four-dimensional minimization procedure that includes coupling of the transverse beam motions. A major requirement is that it obey the restricted lattice design imposed by the acceleration of multiple-charge-state heavy-ion beams. We studied the algorithm efficiency in controlling the beam effective emittance growth in the presence of random misalignments of cavities and focusing elements. Limits on misalignments are determined by quantifying beam losses and effective steering requirements are selected by examining several

correcting schemes within the real state constraints. The algorithm will be used to perform statistically significant simulations to study beam losses under realistic steering.

Algorithm requirements and capabilities:

❖ Control transverse emittance growth: multiple charge states are strongly affected by misalignment errors.
❖ Reduce large trajectory excursions to avoid beam losses.

❖ Respond to the need of frequent machine-settings retuning to accommodate many different ions.

❖ Integral part of TRACK to facilitate beam loss studies in the accelerator.

❖ Capable of being implemented in real machines.

❖ Full 4-D algorithm, includes x-y coupling introduced by solenoids.

❖ Minimization algorithm effective in "many-correctors-to-one- monitor" scenario:

The superconducting driver linac has a large number of components and limited space for diagnostics.

❖ Compares effectively with a "zero-element" correction whereby the beam coordinates as determined "zero-elements", are artificially set to zero. We denote the first as "beam-based" (see Fig. III-10) correction and the second, as "zero-element" (see Fig. III-11) correction.
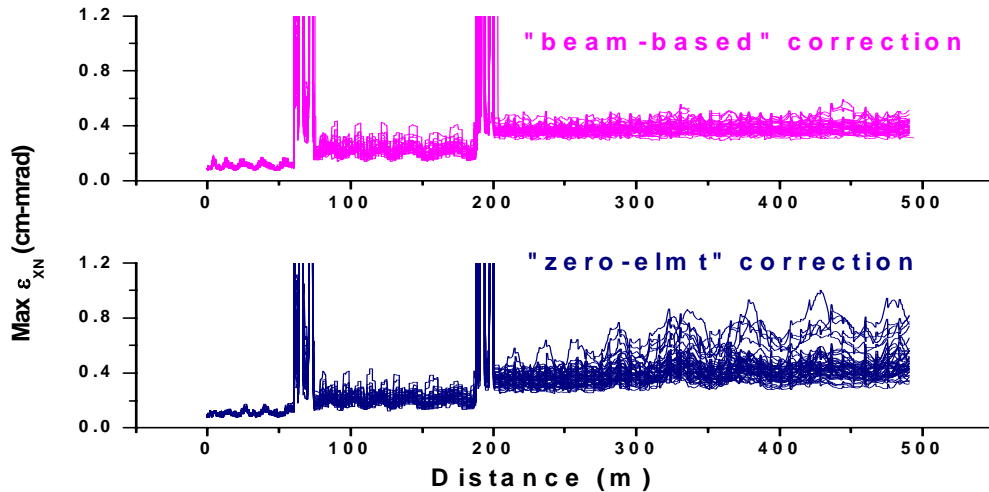

Fig. III-10. "Beam-based"-corrected normalized horizontal emittance for 50 seeds is compared to the corresponding emittance obtained with "zero-element" correction, for 0.05-cm misalignments in solenoids and cavities, and 0.02-cm misalignments in quadrupoles. The spikes at 80 and 180 m correspond to the stripper regions.
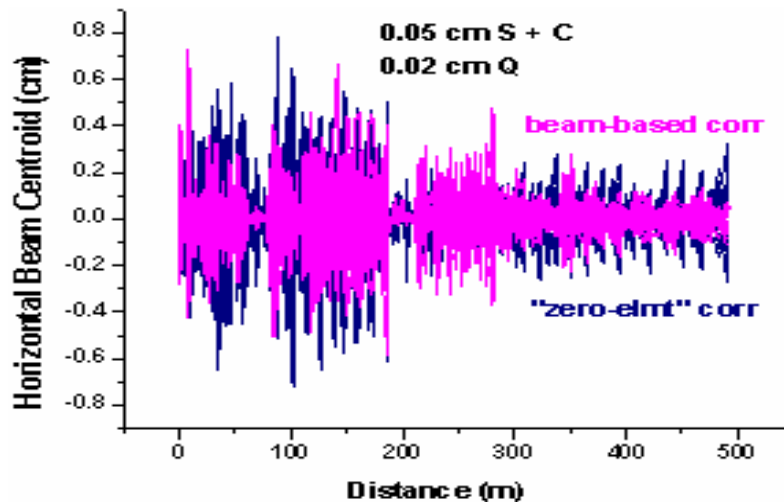

Fig. III-11. Horizontal beam-centroid for misalignment errors, with the beam-based-corrected centroid superimposed on the "zero-element"-corrected centroid. As shown, the beam-based correction reproduces the latter remarkably well. After correction, the oscillations are reduced by 30% to 60%, relative to the uncorrected oscillations, in the lower-energy sections and by 75%, in the high-energy section.

a.7.   Protoype Quarter-Wave and Half-Wave Drift-Tube Superconducting Resonators
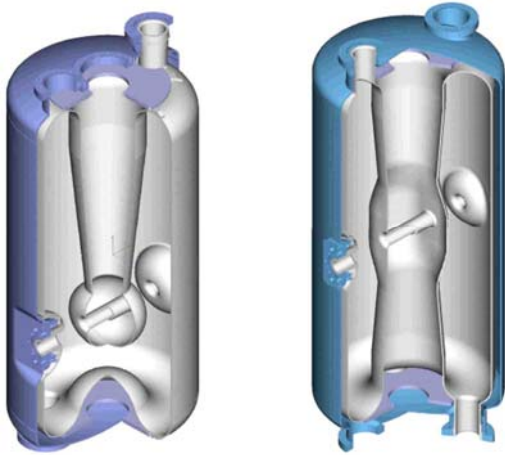(K. W. Shepard, M. Kelly, J. Fuerst, and M. Kedzie)

Fig. III-12. Sectioned views of the 109-MHz quarter wave cavity (left), and the 170-MHz half-wave cavity showing the niobium inner shell, and the outer stainless –steel helium jacket.

Fig. III-13. Niobium elements of the 170-MHz half-wave cavity after electropolishing, but prior to the closure welds.

Development is complete for two types of drift-tube cavity which will be used to upgrade the existing ATLAS linac and which can also be used in the RIA driver linac. Figure III-12 shows sectioned drawings of the cavities, a 109-MHz quarter-wave cavity suitable for particle velocities $0.12 < v/c < 0.25$, and a 170 MHz half-wave cavity suitable for particle velocities $0.25 < v/c < 0.5$. Figure III-13 shows the niobium elements of one of the cavities after electropolishing, which produces a smooth superconducting surface enabling good high-field performance.
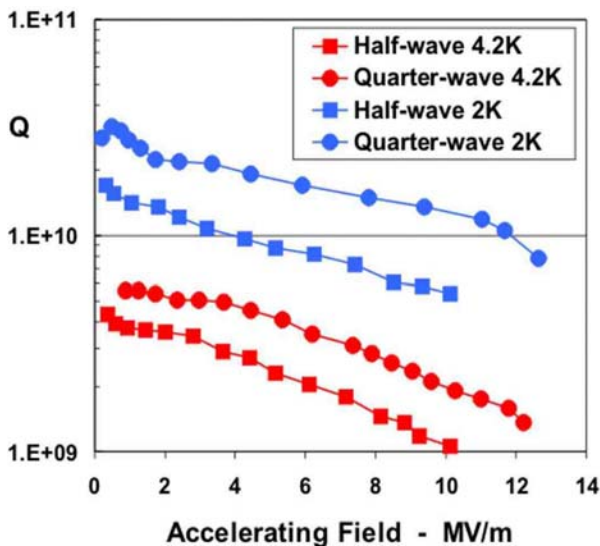

Fig. III-14. Cavity Q as a function of accelerating gradient at 4.2 and 2K.

Figure III-14 details the performance obtained with the prototype cavities, which substantially exceeded expectations. Note that at 4.2 K, the quarter-wave cavity can operate at 12 MV/m, providing 3 MV of accelerating potential with 10 watts of RF input power. The half-wave cavity can provide 2.4 MV of accelerating potential at 4.2 K with 16 watts of RF input. Both cavities exhibited good mechanical stability and observed microphonic-induced phase noise was well within tolerable limits. Several more 109-MHz quarter-wave cavities will be constructed to fill a cryomodule to be used to upgrade the existing ATLAS accelerator.

a.8.   Prototype Cryomodule for Drift-Tube Resonators (K. W. Shepard, M. Kelly, J. Fuerst, and M. Kedzie)

Fig. III-15. Prototype cryomodule vacuum box and top flange being leak-checked.

Design of a prototype cryomodule for the above cavities was completed, and most of the elements fabricated. The cryomodule provides for clean assembly of the cavity string and solenoids. The cavity and cryomodule vacuum systems are separate to enable clean-handling of the critical interior cavity space. The prototype cryomodule is configured to hold eight cavities of the 109-MHz QWR and/or the 170-MHz HWR class, and when complete will be added to the high-energy end of the existing ATLAS accelerator to upgrade the beam energy available from the linac. Figure III-15 shows the recently completed vacuum box with top flange attached being leak-checked at Meyer Tool company.   Figure III-16 shows schematically the cavity string attached to the top-flange of the cryomodule just prior to insertion into the vacuum box.
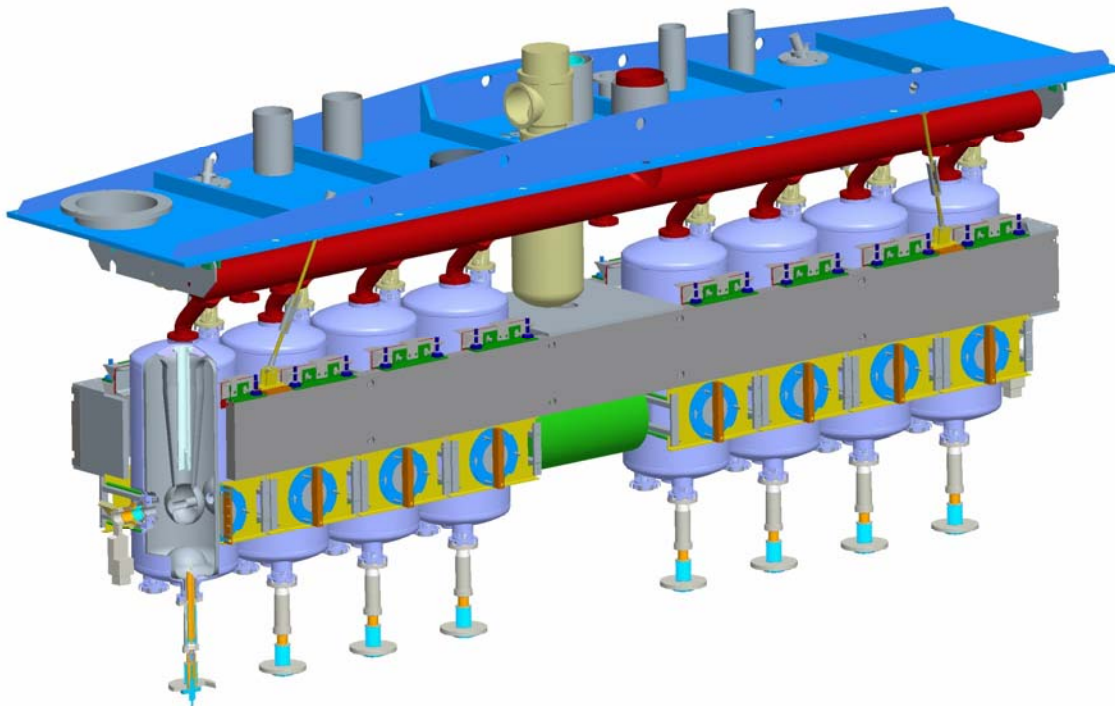

Fig. III-16. Schematic section view of the prototype cryomodule showing the top assembly and attached cavity string assembly, including beam-line valves and rf power couplers.

a.9.   Spoke Cavity Development for RIA (K. W. Shepard, M. Kelly, J. Fuerst, and M. Kedzie)

Cold tests of the prototype double-spoke cavity were completed, as detailed in Figure III-17. The results exceeded the expected performance, and are sufficiently encouraging that development of 345-MHz three-spoke cavities for the high-energy section of the RIA driver linac was undertaken. Construction of two prototype triple-spoke cavities, shown in Fig. III-18, is well-advanced, and initial tests of both prototype cavities are scheduled during 2004.
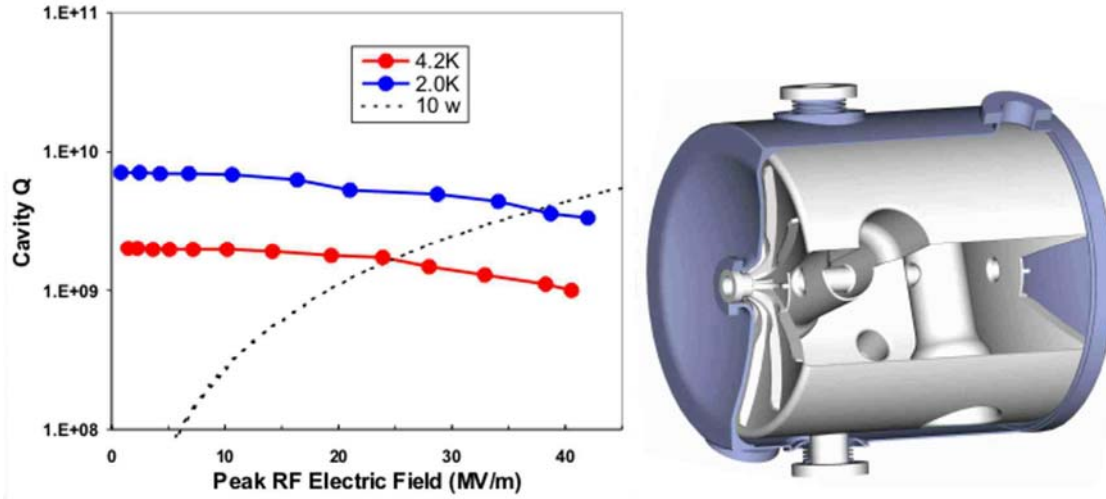

Fig. III-17. Performance of the 345-MHz, $\beta = 0.4$ double-spoke cavity at 4.2K and 2K. At 40-MV/m peak surface electric field, the cavity is operating at an accelerating gradient of 11.5 MV/m and provides some 4.4 MV of accelerating potential.

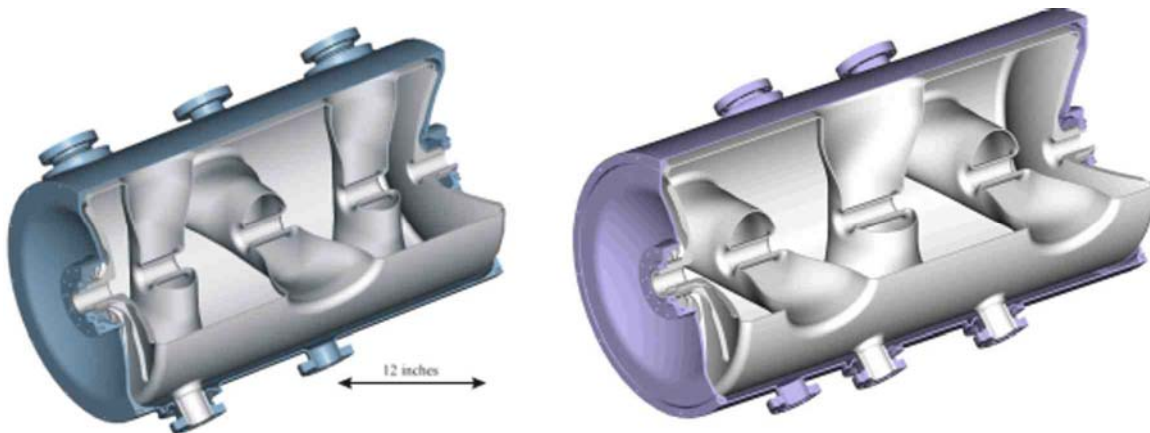| Freq (MHz)	Beta (Geom)	Length (cm)	RF Energy (mJ)	QRs (ohm)	R/Q (ohm)	Epeak (MV/m)	Bpeak (Gauss)
345	0.5	65	397	86	494	2.9	86
345	0.63	81	580	93	520	3	89

Fig. III-18. Triple-spoke cavities for particle velocities $0.4 < \beta < 0.8$ being developed for the high-energy section of the RIA driver linac.

a.10.   Superconducting Linacs for Production of Multi-GeV H⁻ or Proton Beams
(P. N. Ostroumov, K. W. Shepard, and G. W. Foster*)

There is strong demand for proton/H-minus linacs to be used as injectors or drivers for producing high power pulsed beams. Recent proposals include an 8 GeV H-minus linac at Fermilab, a 2 GeV H-minus linac at CERN, an upgrade of the BNL linac to 1.2 GeV, and a proton driver to produce ~100 MW beams for neutron generation.

The successful development of single and double spoke resonators operating at ~350 MHz provides a very strong basis for application of superconducting (SC) low-velocity structures directly after the RFQ section in the above proposed GeV-machines. In addition, the succesful development to date of spoke resonators provides a solid base for the further development of triple-spoke resonators that can used to accelerate protons up to energies of ~400 MeV.   Such development would make it possible to base the front end of a multi-GeV Linac entirely on spoke resonators. Such a front-end would place the transition to higher frequency accelerating structures at 400 MeV, which is highly desirable from a beam dynamics point of view. Currently the technology of high-gradient 1300 MHz SC TESLA cavities with $\beta_G = 1.0$ is well established and can be effectively applied for proton acceleration above ~1.2 GeV. The energy range between 400 MeV and 1.2 GeV can be covered by TESLA-style reduced beta resonators.

We developed a preliminary design for a multi-GeV, entirely SC linac which consists of 6 sections:

conventional RFQ, single-spoke resonators (SSR); double-spoke resonators (DSR), triple-spoke resonators (TSR), squeezed TESLA-type cavities with $\beta_G = 0.81$ and TESLA cavities. The spoke resonators are operated at 325 MHz which is the 4th subharmonic of the TESLA frequency. The voltage gain per cavity along the linac is shown in Fig. III-19.   Table III-3 shows main parameters of the linac. The focusing in the SSR and DSR sections is based on SC solenoids which provide compactness of the focusing lattice. The linac consists of different sections of accelerating and focusing lattice which require appropriate beam matching. Using the TRACK code the beam dynamics simulations of 26 mA H-minus beam represented by 10^5 particles were performed along the entire linac. Although the linac parameters were not optimized for high-intensity beams, the beam dynamics does not reveal any problem. There is ~30% rms emittance growth in the beginning of the linac which can be avoided with equipartioning of the transverse and longitudinal oscillations. The envelopes and evolution of the rms beam emittances along the 8-GeV linac is shown in Fig. III-20.

Our preliminary studies show that the design and construction of high-current proton and H-minus linacs on the base of spoke resonators and TESLA-type cavities is entirely feasible. For the design of the linac for particular application, further optimization of the linac parameters is required to avoid beam halo formation of high-current beams.
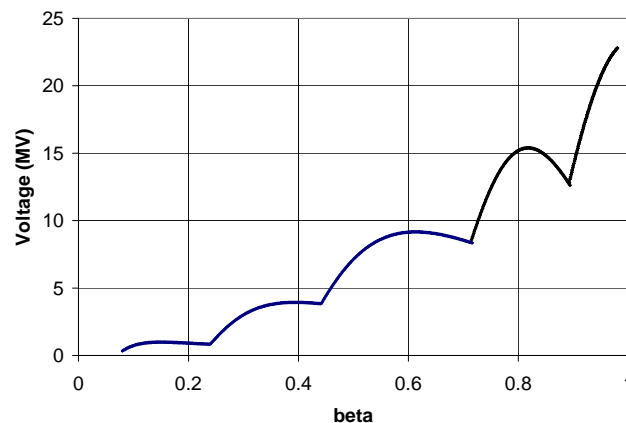

Fig. III-19. Voltage gain (in MV) as a function of proton beam velocity.

---

*Fermi National Accelerator Laboratory.

Table III-3. Main parameters of the 8-GeV H-minus linac.

| Parameter	RFQ	Single-spoke	Double-spoke	Triple spoke	TESLA1	TESLA2
Frequency, MHz	325	325	325	325	1300	1300
Beta geometrical		0.15	0.4	0.61	0.81	1.0
Number of accelerating gaps		2	3	4	8	9
E_{peak}, MV/m		32	32	32	45	45
E_{acc}, MV/m		10.67	10.67	10.67	20.5	22.5
Cavity effective length, cm		9.2	36.9	85.8	74.7	103.8
Number of resonators		34	32	46	56	328
Synchronous phase, deg		-30	-30	-25	-30	-16
Input energy, MeV		3.0	27.8	106	426	1107
Output energy, MeV	3.0	27.8	106	426	1107	8000
Length of the section, m		14.4	33	72	77	553
Maximum coupler power for 26 mA H-minus beam, kW		21.1	88.7	206	346.5	581.4
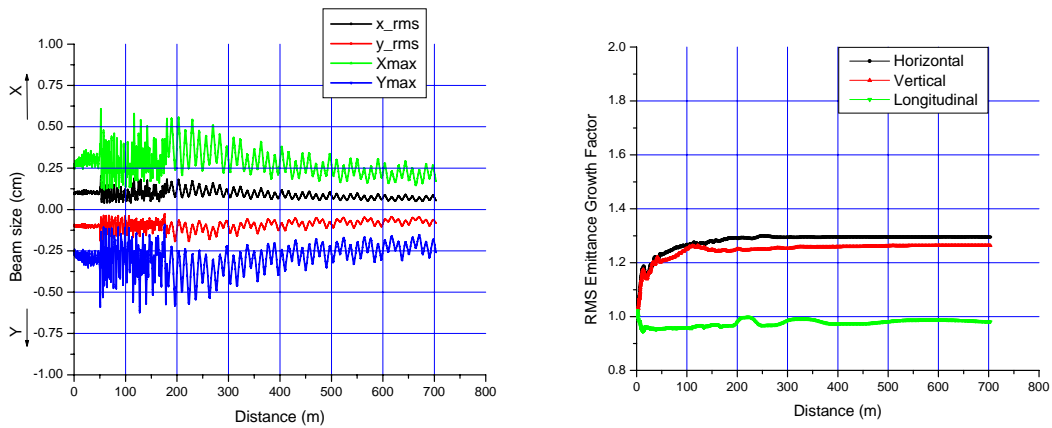
Fig. III-20. Beam envelopes (rms and maximum size) and rms emittances along the linac.

B. RARE ISOTOPE PRODUCTION AND SEPARATION

b.1.   Development of Windowless Liquid Lithium Targets for Fragmentation and Fission of 400-KW Uranium Beams (J. A. Nolen, C. B. Reed, V. J. Novick, Y. Momozaki, P. Plotkin, and J. R. Specht)

Introduction

This section summarizes the on-going development of windowless liquid lithium targets being carried out for the RIA project. The goal of this work is to develop a fragmentation target that can easily work with uranium beams at least up to 100 kW and preferably up to 400 kW, the design limit of RIA. A schematic layout of the proposed concept and the performance goals for the target can be found in last year's report. The beam-spot width is limited to 1 mm due to the optical requirements of the fragment separator. The target thickness is set by matching the energy loss of the beam with the acceptance of the fragment separator.

Behavior of liquid lithium jet irradiated by 1 MeV electron beams up to 20 kW

The high-power heavy-ion beams produced by the Rare Isotope Accelerator (RIA) driver linac have large energy deposition density in solids and in many cases no solid materials would survive the full beam power. Liquid lithium technology was proposed to solve this problem in RIA. Specifically, a windowless target for the production of radioactive ions via fragmentation, consisting of a jet of about 3 cm thickness of flowing liquid lithium, exposed to the beamline vacuum[2,3] is being developed. To demonstrate that power densities equivalent to a 200-kW RIA uranium beam, deposited in the first 4 mm of a flowing lithium jet, can be handled by the windowless target design, a high power 1 MeV Dynamitron was leased and a test stand prepared to demonstrate the target's capability of absorbing and carrying away a 20 kW heat load without disrupting either the 5 mm × 10 mm flowing lithium jet target or the beam line vacuum. Details of justifications on using an electron beam as a thermal load are available elsewhere[1,4,5].   Stable jet formation under beam powers up to 20 kW was confirmed at jet velocities as low as 1.8 m/s. A 55-second beam irradiation at 20 kW resulted in a bulk Li temperature rise of only ~ 30 $^{\circ}$C and a background pressure rise of only ~ 0.3 mTorr. The emissivity of the liquid lithium jet surface was so low that reflections of surrounding emissions dominated and thus temperature readings from an IR camera were unreasonably low.

Experimental layout, setup, and procedure

The experimental setup consisted of the lithium loop, beam line, and Dynamitron electron beam accelerator as shown in Figure III-21. The Dynamitron accelerator, leased from Radiation Dynamics Inc. (RDI), was connected to the loop with the beam line in which the electron beam was delivered to the liquid lithium jet. The beam line was maintained under vacuum at <10^{-6} Torr using a turbo and a diffusion pumps. There were two slight bends in the beam line to prevent any lithium droplets from reaching to the Dynamitron accelerator in the event of lithium jet splashing or disruption. The beam line also had two steering electromagnets to control the beam path.   One magnet controlled horizontal alignment and another controlled vertical alignment of the beam. Gate valves were attached to each end of the beam line to isolate the Dynamitron accelerator and the lithium loop in case of emergencies or maintenance.
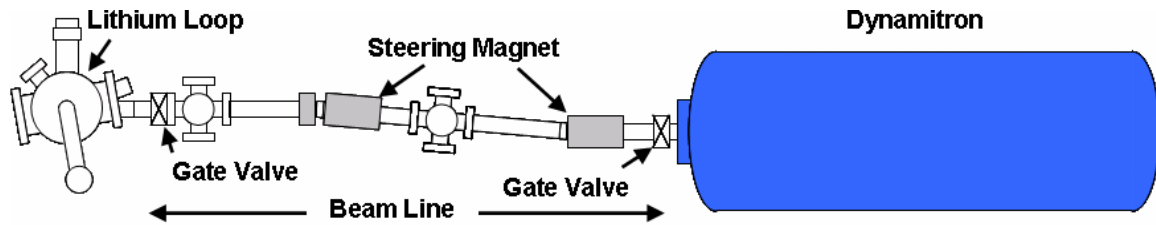
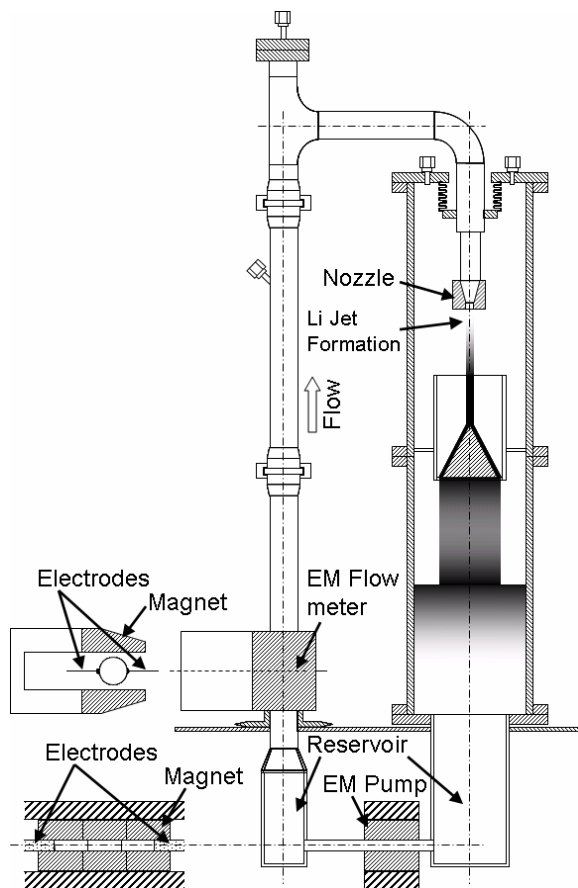Fig. III-21. Schematic top view of experimental layout.

Fig. III-22.   Side view of lithium loop.

The lithium loop was mainly constructed from stainless steel (see Fig. III-22). The loop diffusion pump was capable of maintaining the loop at $< 0.2 \times 10^{-3}$ Torr. The nozzle with an opening of 5 mm in width and 10 mm in depth was located in the vacuum chamber at the downstream of the electromagnetic (EM) flow meter. A free jet of liquid lithium simulating the windowless target was formed at the exit of the nozzle. Ceramic band heaters were attached to the loop to control the temperature. These heaters were connected in five groups, forming five independent zones along the loop and each zone had its own programmable temperature controller. A DC EM pump located at the bottom of the loop as shown in Fig. III-22 was used to circulate the liquid lithium. The EM pump used a pair of permanent magnets (0.746 T) on the top and bottom of the pump ducts. The pump ducts were constructed from the stainless steel and directly welded to the loop to minimize the potential for a leak. Copper electrodes were brazed to each side of the pump and a programmable DC power supply (10 V $\times$ 1000 A) provided DC current to the pump.

Instrumentation

The behavior of the liquid lithium jet was visually observed with a digital camcorder to confirm a stable jet during beam-on heating. The temperatures and the background pressure were monitored to evaluate the capability to handle an extreme thermal load without excessive vaporization.   One mechanically movable, traversing thermocouple (TC) probe was mounted near the jet to measure the temperature distribution across the interior of the jet.   An infrared (IR) camera was used to monitor the surface temperature of the jet.

The applied voltage across the pump was monitored. The pump current was also monitored by means of measuring the voltage drop across a shunt resistor connected in series with the power supply. The loop was also equipped with a DC EM flow meter at the downstream of the EM pump (see Fig. III-22). Using the flow meter, the volumetric flow rate of lithium and the jet velocity at the nozzle were determined as a function of the pump current. The loop had 20, type-K TCs attached at various locations including the EM pump ducts, EM pump magnets, and the EM flow

meter magnet. Data acquisition was controlled by the LabVIEW program. The camcorder was shielded from direct X-ray exposure with lead bricks; the visual images were reflected at right angles using a silver plated mirror located near the viewport. This optical setup was replaced with an IR camera, gold plated mirror, and telescope to observe IR images of the lithium jet for measuring the surface temperature distribution of the jet. These recorded visual images as well as temperatures, pressure, and voltages form the basis of the present work.

Results

Figure III-23 shows the relative location of the jet and beam line as well as the actual image, which correspond a 20 kW run. After confirming stable formation of the jet with low power beams, a series of experiments at increased beam powers up to 20 kW were performed. Due to lack of a heat exchanger in the loop, the duration of each run at high beam power was typically limited to a few minutes. Figure III-24 shows the history of measured temperatures at the nozzle and the splash shield, and background pressure taken at the highest beam power of 20 kW.
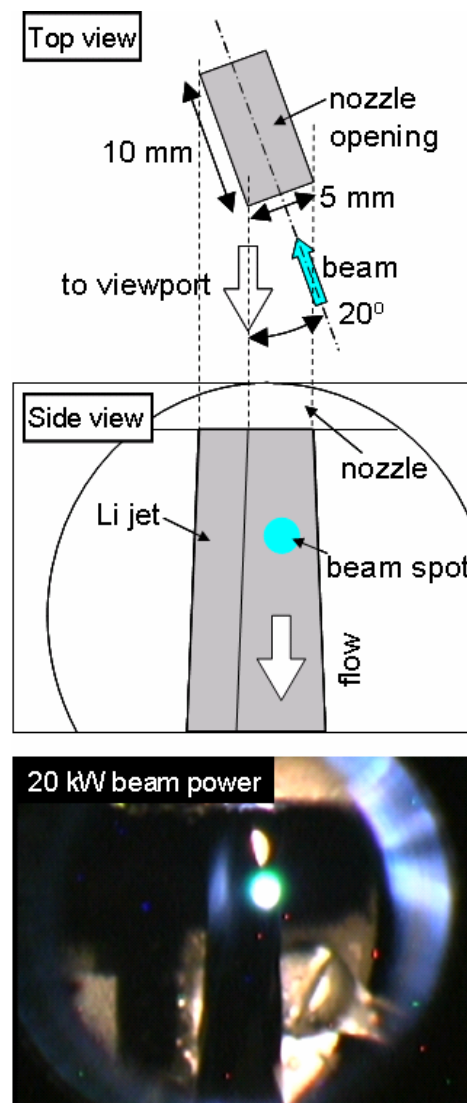

Fig. III-23. Schematic of nozzle, jet, and beam and actual image of jet at 20 kW beam power.

The pump current was kept at 200 A at which the estimated jet velocity was about 1.8 m/s. The beam power was increased quickly (20 kW over ~30 seconds) to minimize the temperature rise in the system.

As a result, a steady beam power of 20 kW was achieved for about 55 seconds. A steady, 55 seconds of electron beam irradiation at 20 kW resulted in a temperature rise of ~30°C in bulk lithium temperature. Observed increase in pressure was only ~0.3 mTorr (from 0.8 to 1.1 mTorr) during this experiment.
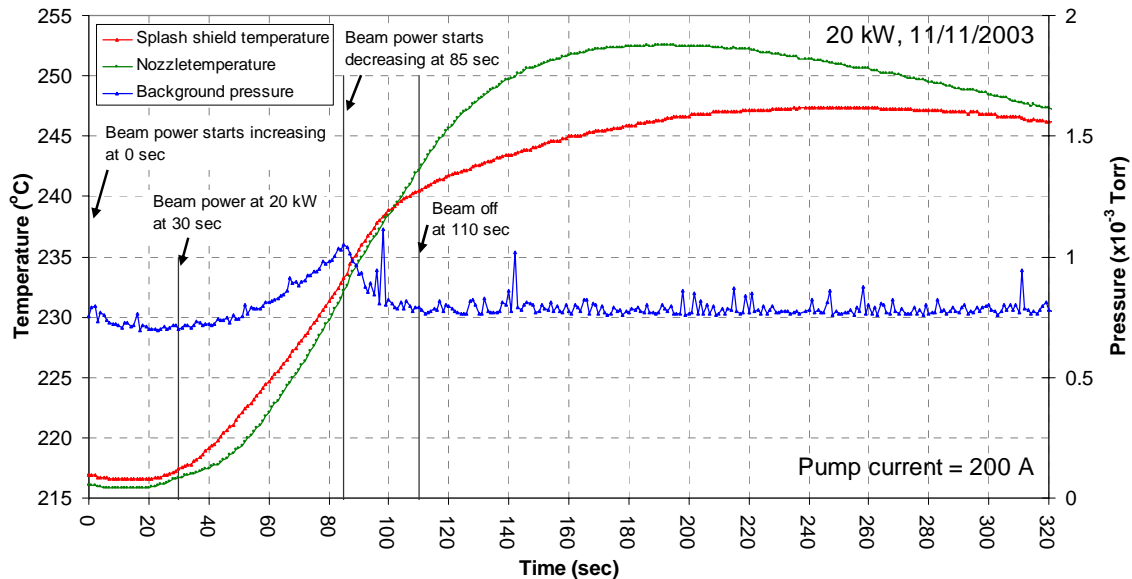

Fig. III-24. Temperature and pressure during 20 kW test.

Summary and conclusions

Experiments were performed to demonstrate the stable formation of a liquid lithium jet that simulated the windowless liquid lithium target under a thermal load similar to that of RIA using a 1 MeV electron beam. Stable jet formation under the beam powers up to 20 kW were confirmed at the jet velocity as low as 1.8 m/s. A 55 second beam irradiation at 20 kW resulted in a temperature rise of only ~30°C in bulk lithium temperature and a background pressure rise of only ~0.3 mTorr. Attempts to measure the spatial temperature distribution across the jet were also made using a traversing TC and an IR camera, however, emitted X-ray internally heated up the tip of the TC, resulting in inaccurate temperature measurements. The emissivity of the liquid lithium jet surface was so low that reflections of surrounding emissions dominated and thus temperature readings from an IR camera were unreasonably low.

_____

[1]Gomes, I. C., Nolen, J. A., and Reed, C. B., "The Use of Electron Beams in RIA R&D," 2002.

[2]Nolen, J. A., "The U.S. Rare Isotope Accelerator Project," Invited paper at the XXI International Linac Conference, Aug. 19-23, 2002.

[3]Nolen, J. A., Reed, C. B., Hassanein, A., and Gomes, I. C., "Liquid-lithium cooling for 100-kW ISOL and fragmentation targets," Nucl. Phys. **A701**, 312c-322c, 2002.

[4]Reed, C. B., Nolen, J. A., Specht, J. R., and Novick, V. J., "Engineering and Safety Issues of Lithium Targets and Film Strippers," AccApp 2003 Proceedings, ANS, 2003.

[5]Reed, C. B., Nolen, J. A., Specht, Novick, V. J., and Plotkin, P., "A 20 kW Beam-on-Target Test of a High-Power Liquid Lithium Target for RIA," RNB6, 2003.

b.2.   Development and Testing of the Full-Scale RIA Gas Catcher Prototype

(G. Savard, W. Trimble, J. Clark* F. Buchinger,† T. Coccolios, J. E. Crawford,†
A. Frankel, J. P. Greene, S. Gulick, J.K.P. Lee,* A Levand, M. Maier,‡
D. Seweryniak, K. S. Sharma,* J.C. Wang,* B. J. Zabransky, Z. Zho,
and the S258 Collaboration)

The gas catcher system is a key component of the RIA facility, providing access to low-energy beams of short-lived isotopes not amenable to the standard ISOL technique. The gas catcher concept for RIA is a new approach to the extraction of radioactive ions that was proposed in 1998 based on developments at lower energy at the CPT spectrometer at Argonne. The gas catcher stops fast recoils in high purity helium and uses a combination of DC and RF electric fields together with gas flow to obtain high efficiency and short delay times in the extraction of the radioactive ions. Since then significant R&D efforts have been invested at Argonne to yield a design scalable to the 0.5 atmosphere-meter stopping power of helium required for RIA. The RIA gas cell R&D efforts performed at Argonne in FY2000-FY2001 resulted in the demonstration of a ¼ scale prototype gas cell geometry capable of operating with 45% efficiency, more than double that originally specified for RIA. Possible limitations of the technology we developed were investigated and the solution selected for RIA and resulting predicted yield seem robust. In the latter part of FY2001 and in FY2002 we designed and completed the construction of a full-scale RIA gas cell prototype, fulfilling a DOE/NP performance milestone for FY2002. The prototype is a scaled up version of the previous prototype, built with particular emphasis on maintaining gas purity which was found to be an important contributor to our previous prototype's success this far and which becomes a much more difficult task as the surface area inside the device becomes larger and larger. We achieved our purity goals with UHV techniques applied to the construction and assembly of over 4000 of the 7400 components of the gas catcher system. The prototype was tested successfully and characterized with low energy radioactive beams at Argonne during most of FY2003. We are satisfied with the results obtained at low energy and are now preparing to move the device to GSI where it will be installed behind the FRS fragment separator

for on-line tests at the full RIA energy. This will fulfill a DOE/NP performance target for FY2003.

The gas catcher concept developed at Argonne uses a combination of DC and RF fields superposed on top of gas flow to extract effectively and quickly short-lived isotopes stopped in the high-purity helium gas. The combination of the three forces provides fast transport through the main part of the device (DC field), focusing towards the extraction nozzle (RF field) and rapid extraction through the nozzle (gas flow). It allows one to use much larger stopping gas volume than gas flow alone and to handle much higher intensity than DC field based system (the first such DC system was developed by us in 1998 and obtained about 20% efficiency at low intensity but saturated at very low ionization level, a problem inherent to all DC only designs proposed so far).

The mechanical construction and assembly of the full-scale RIA gas catcher prototype, with its more than 7400 components, was completed in August 2002. The assembled full system was vacuum tested and baked and found to have an outgassing rate sufficiently low to maintain the ppb level purity of the helium gas under normal operating conditions (a non-trivial task for a system that large with essentially no pumping speed in normal operation). The next step was construction and installation of tuned circuits to provide the required RF and DC voltages. Figure III-25 presents the fully assembled gas catcher system with tuned circuits providing the DC and RF fields installed. The capacitance of the cone (278 plates separated by 0.015") is 97 nF which required significant RF power to generate the design RF amplitude but the task was completed successfully with an air-core inductance to tune the RF tank circuit and tolerate the stored RF power. The system was tested to full RF power and DC voltage specifications. The gas catcher system was installed in a high-voltage cage on a very rigid movable platform that hosts it throughout its displacements.
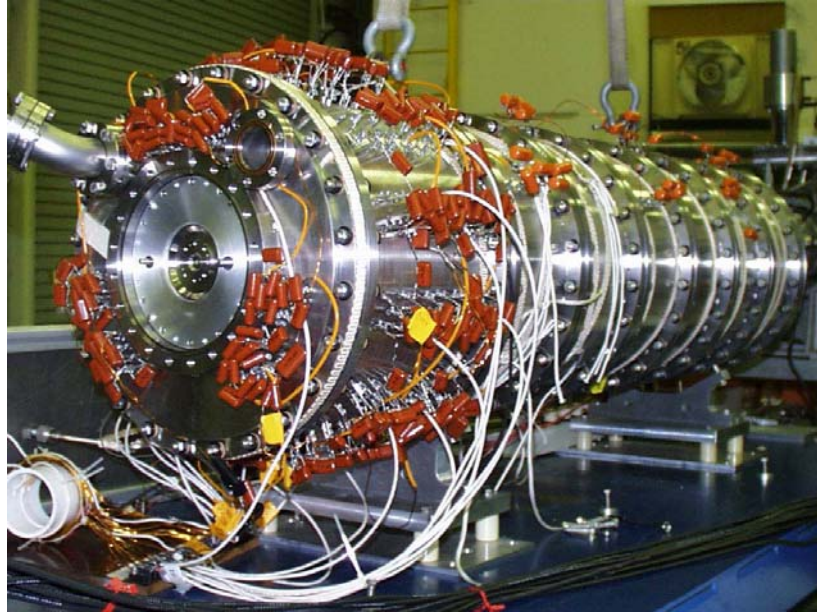
_____

Fig. III-25. Assembled RIA gas catcher prototype with tuned circuit to provide RF and DC potentials to the body and cone electrodes. The extraction nozzle and chamber hosting the extraction cone can be seen on the left side of the picture.

The completed gas catcher prototype was moved to the general purpose experimental area at the ATLAS superconducting linac accelerator at Argonne for testing. A diagnostic station composed of two sections of RFQ quadrupole separated by differential pumping apertures and followed by a time-of-flight drift section terminated by movable MCP and Si detectors was built and connected to the extraction nozzle of the gas catcher (see Fig. III-26). This allowed counting of the extracted radioactivity with the Si detector to yield absolute total efficiency, identification of the extracted ions by time-of-flight technique with the MCP detector, and mass-gated counting of the activity by opening a transmission gate in the time-of-flight system to let only ions in a specific mass range go through and then detect the mass selected activity with the Si detector. The initial section of RFQ was pumped by a clean booster pump backed by a large rotary pump, the second RFQ section and drift section were pumped by turbo pumps. Pressure in the gas catcher system was measured by an all-metal capacitance manometer and an all-metal valve

was used as a bypass between the gas catcher and the first RFQ section for pumping down the device when not in operation or during bakeout. Heating tapes on the gas catcher vacuum system allowed the device to be baked regularly to about 80 C (to stay well below the 125 C melting point of the Indium seals). A problem with breaking of large insulating Alumina rings in the gas catcher when heated was eliminated by a redesign of the rings to minimize concentration of expansion stress and assembly of the device under elevated temperature to preload the rings. The gas catcher was connected to the ATLAS beam line via a ceramic insulating section and the vacuum isolated by a 3.1 mg/cm^2 HAVAR window supported by a 90% transmission stainless steel grid. A bypass pumping valve was incorporated between the ATLAS beamline and the first section of RFQ (which can be bypassed to the gas catcher) to minimize differential pressure across the gas catcher window during pumping down of the system.

MCP / Si detectors

Linear Paul trap

RFQ Sec 2

RFQ Sec 1

Gas-filled Extraction Cone + cell
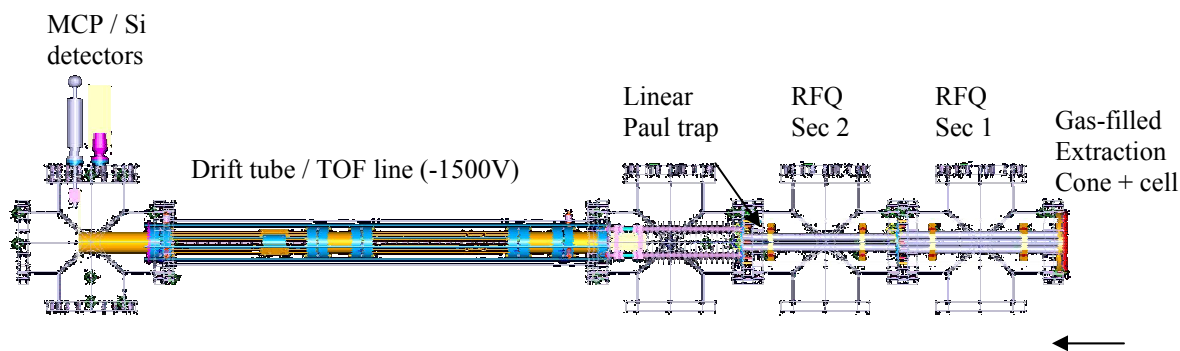
Drift tube / TOF line (-1500V)

Fig. III-26. Layout of the extraction system connected to the nozzle of the gas catcher system and the diagnostics station used to identify the extracted ions and count the extracted activity.

Two techniques were used to inject radioactive ions in the gas catcher. First, a 5 μCi ^{252}Cf source was installed on the entrance window of the gas catcher system. This source provides a constant known source of short-lived isotopes of various chemical species between mass 95 and 150 and recoil energies between 90 and 140 MeV. This source was used extensively to determine initial operating parameters for the device and perform systematic studies on stopping in the gas, charge state distribution and total and partial yield dependency on operating parameters. A second approach involved the production of short-lived isotopes by reaction of a high-intensity heavy-ion beam from the ATLAS accelerator with a cryogenic gas target, focusing of the reaction products with a superconducting solenoid, energy focusing with a superconducting resonator followed by a rough selection in a bending magnet. This technique was used to inject isotopes of ^{37}K ($t_{1/2}$ = 1.2 s) and ^{25}Al ($t_{1/2}$ = 7 s) in the gas catcher. The total ion flux reaching the gas catcher was measured with a movable Si detector and attenuators. The fairly good properties of the secondary beam allowed the position where the ions stopped in the gas catcher to be changed with variable thickness degraders installed on a target ladder located in front of the gas catcher entrance window.

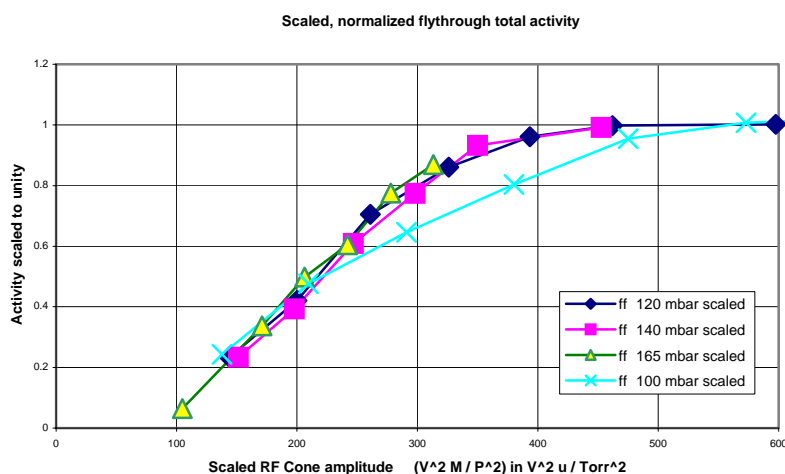
Scaled, normalized flythrough total activity

Fig. III-27. Normalized mass-gated activity extracted from the gas catcher system as a function of the effective RF focusing force exerted by the RF cone. The RF force calculated scaling yields essentially a universal curve in agreement with our simulations.

Various tests were performed on the gas catcher system with these two sources of radioactive ions. The main goals were to determine the efficiency of the device and demonstrate that the device behaved as calculated under various operating conditions. The effectiveness of the RF focusing and its scaling was demonstrated by studying the fraction of extracted activity versus RF focusing amplitude for various pressure and isotope mass regimes. A typical plot for fission fragments extracted under various pressure conditions in the gas

catcher is shown in Fig. III-27. An essentially universal curve is obtained which agrees with our simulations. Data from other radioactive species obtained both on-line and off-line confirms the agreement. The behavior of the extraction efficiency versus stopping position inside the gas catcher is best determined with the on-line produced radioactive isotopes which can be stopped in well defined location along the length of the gas catcher. The result of such a study is shown in Fig. III-28 for radioactive ions of ^{37}K. The efficiency along the gas catcher system is essentially constant over a wide range of operating parameters.
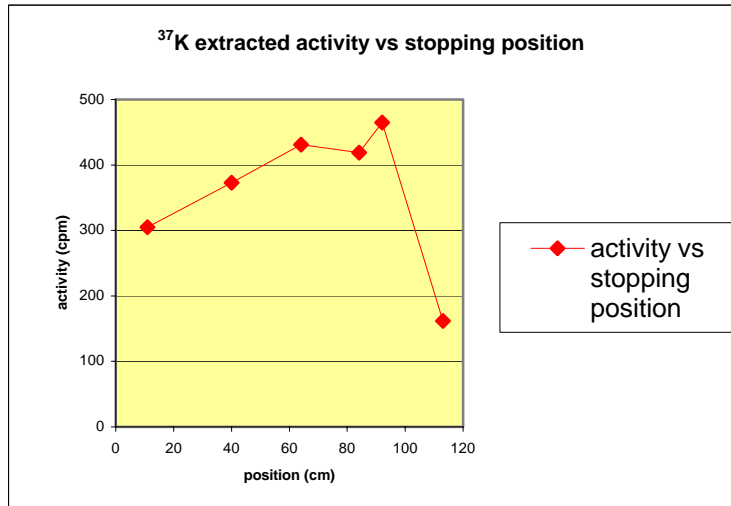

Fig. III-28 ^{37}K *activity extracted from the gas catcher system as a function of the position along the gas catcher where the activity was stopped. The stopping position was varied by changing the thickness of a degrader in the ATLAS beamline.*

The exact form in which the activity is extracted is obviously also of interest. We used the time-of-flight identification of the activity to verify that the radioactive ions were extracted as ions and not as molecular ions or adducts. In our on-line experiments with ^{37}K we determined that within experimental uncertainty all activity was extracted at a mass to charge ratio below 40. From this we can conclude that at least 95% of the activity is extracted as singly charged ions for these light ions produced on-line. In our fission fragment studies, we also determined that essentially all activity is extracted as ions but we found a mixture of singly-charged and doubly-charged ions for most of the heavy fragments (similar behavior has been observed in our CPT gas catcher system and use to an advantage there in measurements on heavy fission fragments). The fraction of doubly-charged ions depends on the operating conditions and this behavior is still being investigated.

The total efficiency of the system was obtained under various conditions. An efficiency of about 40% was obtained for fission fragments stopped in the gas catcher. That is consistent with results obtained at our smaller scale CPT gas catcher. That efficiency can be maintained up to the maximum pressure the pumping system in the test stand at Argonne can tolerate which is just above 200 mbar (the pumping system will be upgraded when funds are available). For the lighter species produced in our on-line tests we obtained efficiencies between 10% and 35% depending on operating parameters. In particular, the RF amplitude required on the RF cone to obtain the highest efficiencies for light ions exceeds our RF capabilities at this point. For example, we obtained 35% efficiency for ^{37}K at 120 mbar but that number drops to about 20% at 160 mbar. That behavior is in agreement with our modeling of the RF focusing force and the situation can be improved with a technique we are developing to apply higher RF amplitude to the cone structure.

We also investigated the effect of space charge on the efficiency and do not see any effect within the range of ionization density that was studied. These measurements were performed on-line and have been extended to ~5×10^5 particles per second entering the gas catcher. These investigations must be continued at higher intensities and that work will be continued at Argonne with a second prototype gas catcher.

We are satisfied with the results obtained at low-energy with the gas catcher prototype and the device was moved to GSI for operation behind the FRS fragment separator there. A more powerful pumping system was commissioned there that will allow operation at higher pressure than what could be done at Argonne. The large roots blower system was tested and an analysis of the residual gas above the roots blower was satisfactorily completed. All electronics of the gas cell was purchased

to be easily convertible from the local 120V 60 Hz power to the 220V 50 Hz European standard and was easily reinstalled there.

The site preparation at GSI involved the installation of a test stand for off-line preparation of the device and design of a stand to install the gas catcher behind the FRS in a space compatible with the RISING project which has a germanium detector array installed at the focal plane of the FRS. The solution selected is depicted in Fig. III-29. The preparation of the FRS for operation as an energy buncher for the reaction residues has been tested already in previous years and the mode of operation selected for the gas catcher will use the target to S3 part of the separator has a separator while the S3 to S4 section will be used as a range buncher. The newly developed glass degrader with optical quality tilted surfaces that provide the required degrader homogeneity will be used. Beam time is approved (but not yet scheduled) at GSI for the gas catcher tests.

These tests will demonstrate operation at the RIA energy and allow us to identify possible improvements

to our approach. The main remaining uncertainty attached to the gas catcher system after these tests will be the maximum intensity that the device can tolerate. Testing the high-intensity limits of the device and determining how to best push them further will be a time consuming task that is best done at the ATLAS facility. We built from spares the main components of a second gas catcher prototype that will remain at Argonne. We plan to investigate over the coming years the intensity limits of the device: determine the actual present limits (instead of extrapolating from lower intensity which is all we were able to do this far) and find the best approaches to raise these limits to higher levels. It can be shown that the approach used here for the gas catcher can handle much higher intensity than a DC only approach. It can just as easily be shown that RIA can in certain circumstances produce more activity than even our approach can handle. These high intensity studies should therefore be a very high priority item in the RIA R&D list.
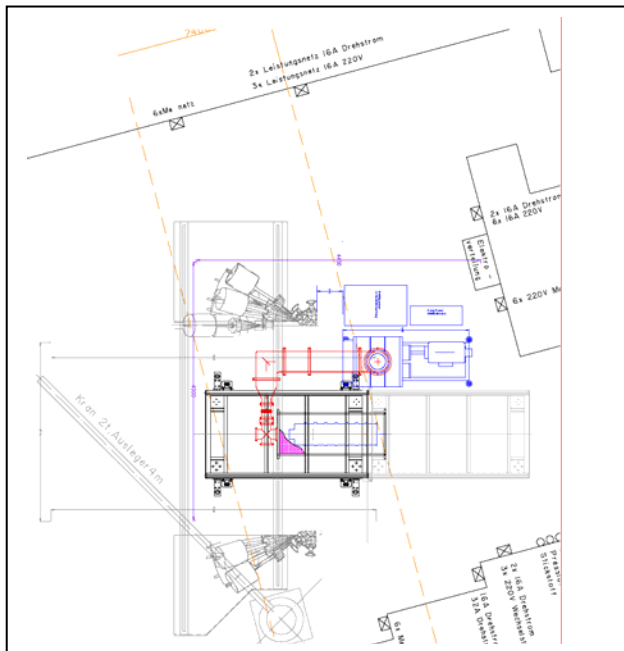

Fig. III-29. Layout of the gas catcher system at the focal plane of the FRS. The gas catcher is resting on a movable frame which fits between both halves of the RISING detector array. The large roots blower pump is located besides the support frame and the high-conductance pumping line is shown in red in the drawing.

b.3. Yield Calculations for a 400-kW RIA Accelerator Facility (C. L. Jiang, B. B. Back, J. Nolen, K. E. Rehm, G. Savard, and J. P. Schiffer)

In the past years, yield calculations were done for an advanced rare isotope accelerator facility.[1,2] Most of these calculations were devoted to a 100-kW, 400-MeV/u facility. In the design study of the linac driver accelerator, it was found that the machine could be easily expanded to a 400-kW design.[3] New calculations for such a RIA facility were carried out. Two contour plots are shown in Figures III-30 and III-31 for re-accelerated beam and fast beam, respectively. The last one was referenced in the report of the NSAC Subcommittee.[4] These yield calculations were extended to the order of 10^{-6} particles/s. Two r-process lines are included in the plots (came from different theoretical calculations) for references. Other calculations of production yields, like either of re-accelerated beams or of fast beams as function of the mass number for every element ($2 < Z < 92$), are renewed and available.

---

[1]C. L. Jiang, B. Back, I. Gomes, A. M. Heinz, J. Nolen, K. E. Rehm, G. Savard, and J. P. Schiffer, Physics Division Annual Report 2000, Argonne National Laboratory, p. 75 (2000).

[2]C. L. Jiang, B. Back, I. Gomes, A. M. Heinz, J. Nolen, K. E. Rehm, G. Savard, and J. P. Schiffer, Nucl. Instrum. Methods **A492**, 57 (2002).

[3]J. Nolen, "Overview of the U.S. Rare Isotope Accelerator Proposal", to be published in the proceedings of the Nucleus-Nucleus Collision Conference, Moscow, Russia, June 17-21, 2003.

[4]Report of the NSAC Subcommittee on "Comparison of the Rare Isotope Accelerator (RIA) and Gesellschaft für Schwerionenforschung (GSI) Facility Upgrade", Feb. 9, 2004.
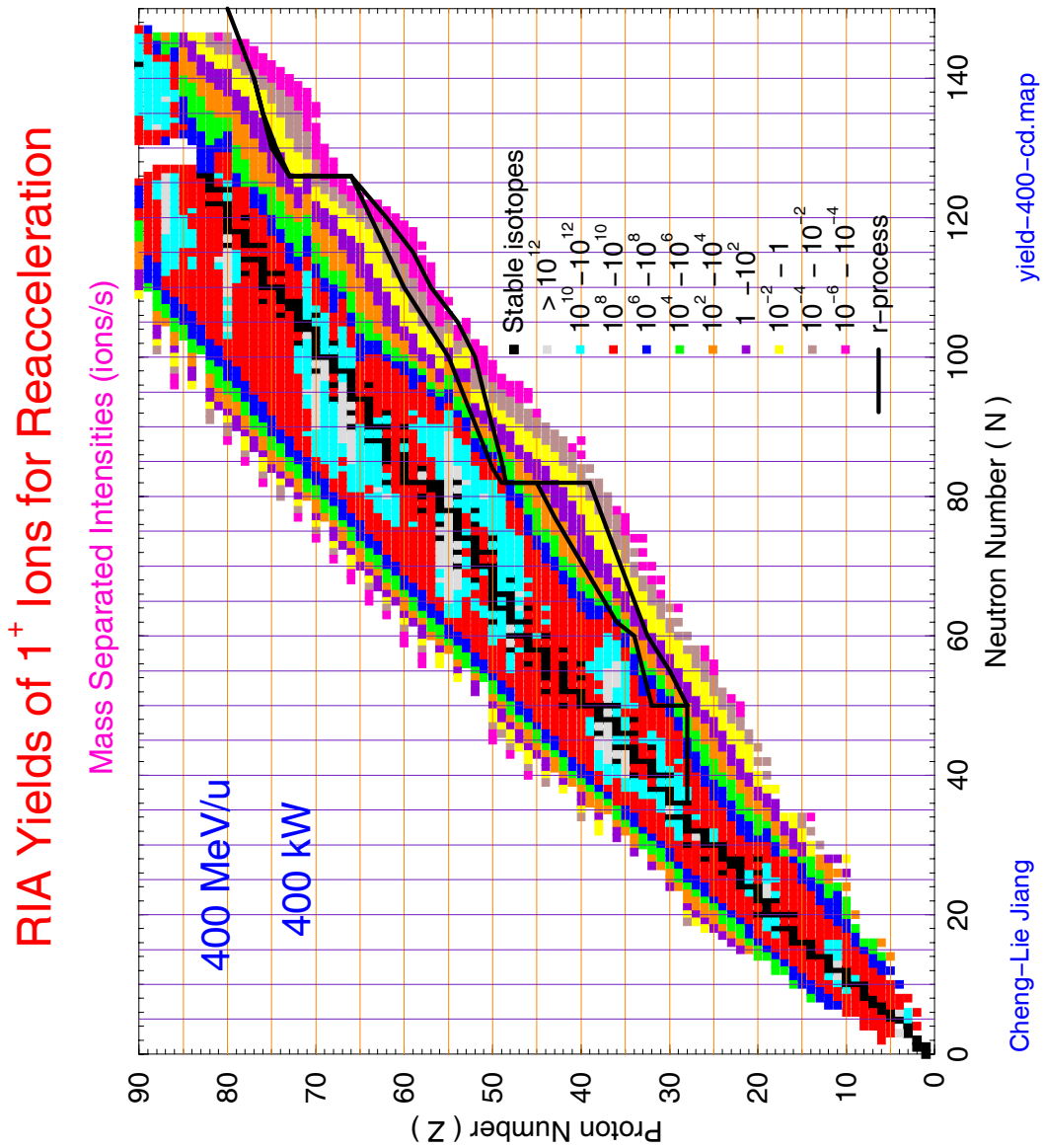
Fig. III-30. Contour map of isotopes yields calculated for reaccelerated beams produced with a 400-kW, 400-MeV/u primary beam driver. The map extends to isotopes for which the yield would be of the order of 10^{-6} particles/s. Products produced from in-flight fission or projectile fragmentation are required to have lifetimes >1 ms and a momentum dispersion $< \pm 9\%$.
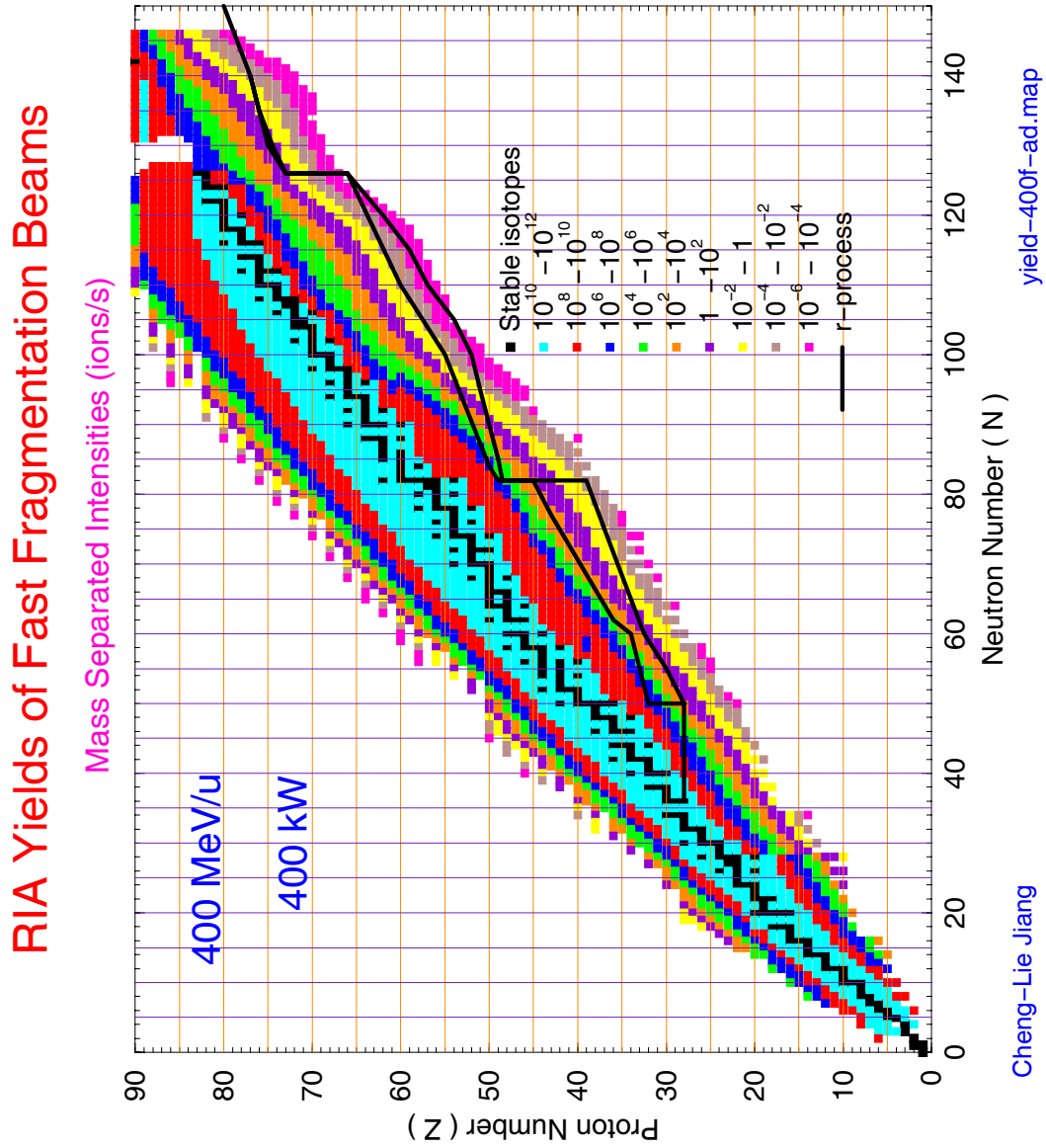
Fig. III-31. Contour map of isotopes yields available for prompt, high-energy beams (150 - 350 MeV/u) produced with a 400-kW, 400-MeV/u primary beam. The map extends to isotopes for which the yield would be of the order of 10^{-6} particles/s. Products are required to have lifetimes >1 μs and a momentum dispersion < ±3%. A few isotopes with shorter lifetime near N = 128 - 130 are indicated (white area).

b.4.   The Influence of Secondary Reactions in the Wedge of a Magnetic Separator at RIA

(C. L. Jiang, B. B. Back, J. Nolen, K. E. Rehm, and G. Savard)

The isotopic contamination of secondary beams produced at a next generation rare isotope accelerator is a critical issue. In a recent paper, calculations of secondary beam intensities for such a facility were published.[1] For each radioactive beam, the primary beam and the thickness of the liquid lithium production target have to be optimized in order to achieve high yields. However, the contamination of the secondary beam was not discussed in that paper. In this contribution we discuss the question of beam contamination for isotopes produced via the fragmentation or in-flight-fission techniques. These calculations provide important information for minimizing the contamination in a magnetic-separator or in other ion optical systems.

For the fragmentation and uranium-fission reaction methods for both fast and re-accelerated beams, the reaction products from the target all feed into the separator system, which is set to select the requested beam. A majority of these products can pass through the separator system and become contaminants since they may have a similar magnetic rigidity to the requested beam. An energy-compensation wedge is often used inside the separator to reduce these contaminants, because this wedge causes a momentum shift that is different from that of the requested beam. In all experiments carried out thus far, the targets and wedges used are thinner than what will be used in the RIA facility. However, in order to get the highest intensity of the secondary beam in the next generation rare isotope accelerator (RIA), especially for the most exotic nuclei, a thicker target (around several g/cm^2 liquid lithium) and a thick wedge (for purification) are required. As a consequence, we found that secondary reactions induced by the primary contaminants in the wedge must be considered. In addition, the configuration and optical parameters of the magnetic separator system are found to play critical roles for the suppression of beam contaminants, especially for these thick production targets and wedges.

A set of computer codes was developed to calculate the contaminants originating from the target and the energy compensation wedge in the magnetic separator system. In these calculations, all reaction products produced at the target, within the same magnetic rigidity range as the requested beam, are followed through the separator, taking into account secondary reaction products produced at the wedge. A method was developed to simplify these multi-particle, multi-parameter and multi-process calculations. An incremental value of

$\Delta(B\rho)$ was introduced to simulate the total effects of energy straggling and small angle scattering in the target and in the wedge. That is, a specific incremental value $\Delta(B\rho)$ is added to the $(B\rho)$ value for each kind of reaction products exiting the wedge. It is then possible to determine, which part of the primary and secondary contaminants can pass through the separator system.

An example is shown in Fig. III-32 for a secondary ^{78}Ni beam produced via the fragmentation technique from a 400-MeV/u, 100-kW ^{86}Kr beam. The ^{7}Li target used is 3 g/cm^2, the total fragmentation product rate is about $3.5 \cdot 10^{12}$/sec, in comparison to the requested ^{78}Ni yields produced at only about 10/sec. After the selection by the first part of the separator (using $\dfrac{\Delta(B\rho)}{B\rho} = \pm 4.2\%$),

contaminants produced at a rate of about $2.9 \cdot 10^9$/sec, which have the same magnetic rigidity range as the ^{78}Ni beam, are transported through the first part of the separator and impinge on the wedge along with the ^{78}Ni ions. By varying the thickness of the wedge and tuning the settings of the second part of the separator, the contaminants can be reduced by a factor of several orders of magnitude, but not totally eliminated. The computer program LISE++.version 6.x^2 may be used to calculate the fragmentation products passing through a magnetic system. This program, however, does not include the reactions in the wedge. The dashed curve in Fig. III-32 represents the yield of ^{78}Ni as a function of the thickness of the Al wedge obtained using this program. Including the reactions induced by the primary contaminants in the wedge, which are not included in the LISE calculations, results in the production of new contaminants, the intensity of which increase with the thickness of the wedge. These contaminants will be transmitted through the second part of the separator along with the ^{78}Ni beam (solid curve in Fig. III-32).

A two-dimensional Z-N contour plot of contaminants without the wedge is shown in Fig. III-33, together with drip lines and the stable isotopes for comparison. The contaminations with an Aluminum wedge of thickness 4.9 g/cm^2 are shown in Fig. III-34. It is evident that using a wedge reduces the contaminant level and shifts them to the less proton rich domain. Clearly, another separator and wedge section is needed in order to further purify the ^{78}Ni beam. The calculations, which include the reactions in a second wedge, are in progress.

A similar calculation for ^{138}Sn, produced via the in-flight fission technique, is shown in Fig. III-35. The target used here is a relatively thin 0.5 g/cm^2 liquid Lithium in order to illustrate the target thickness dependence (as compared with Fig. III-32).

In summary, the influence of the energy compensation wedge on the level of beam contaminants is two fold.

The effect of energy loss difference for various isotopes reduces the contamination level, but the secondary reaction products generated in the wedge introduces new beam contaminants. This latter effect becomes dominant for the very weak channels, which will become available at more powerful facilities. Thus the design of the separator system and the thickness of the wedges need to be optimized carefully.

_____

[1] C. L. Jiang, B. B. Back, I. Gomes, A. M. Heinz, J. Nolen, K. E. Rehm, G. Savard, J. P. Schiffer, Nucl. Instrum. Methods **A492**, 57 (2002).

[2] O. Tarasov *et al.*, Nucl. Phys. **A701**, 661c (2002); D. Bazin *et al.*, to be published; Web site-http://group.nscl.msu.edu/lise/lise.html.
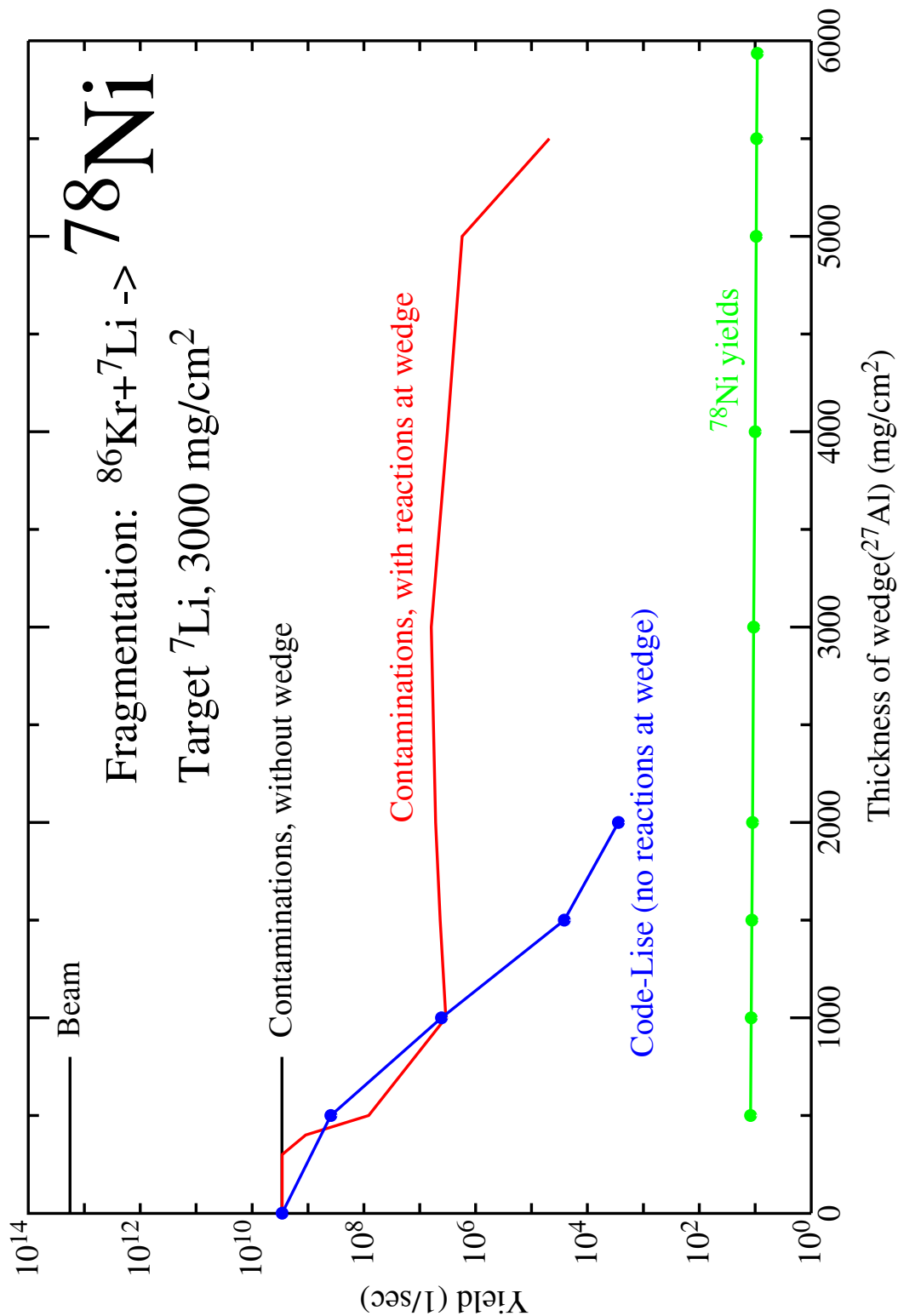
Fig .III-32.   *The beam contaminant yields computed with (solid curve) and without (dashed curve) including reactions in the wedge is compared to the ^{78}Ni yield (dotted curve) produced via fragmentation of a 400 MeV/u, 100 kW ^{86}Kr primary beam on a 3 g/cm^2 ^{7}Li target as a function of the thickness of the wedge.*
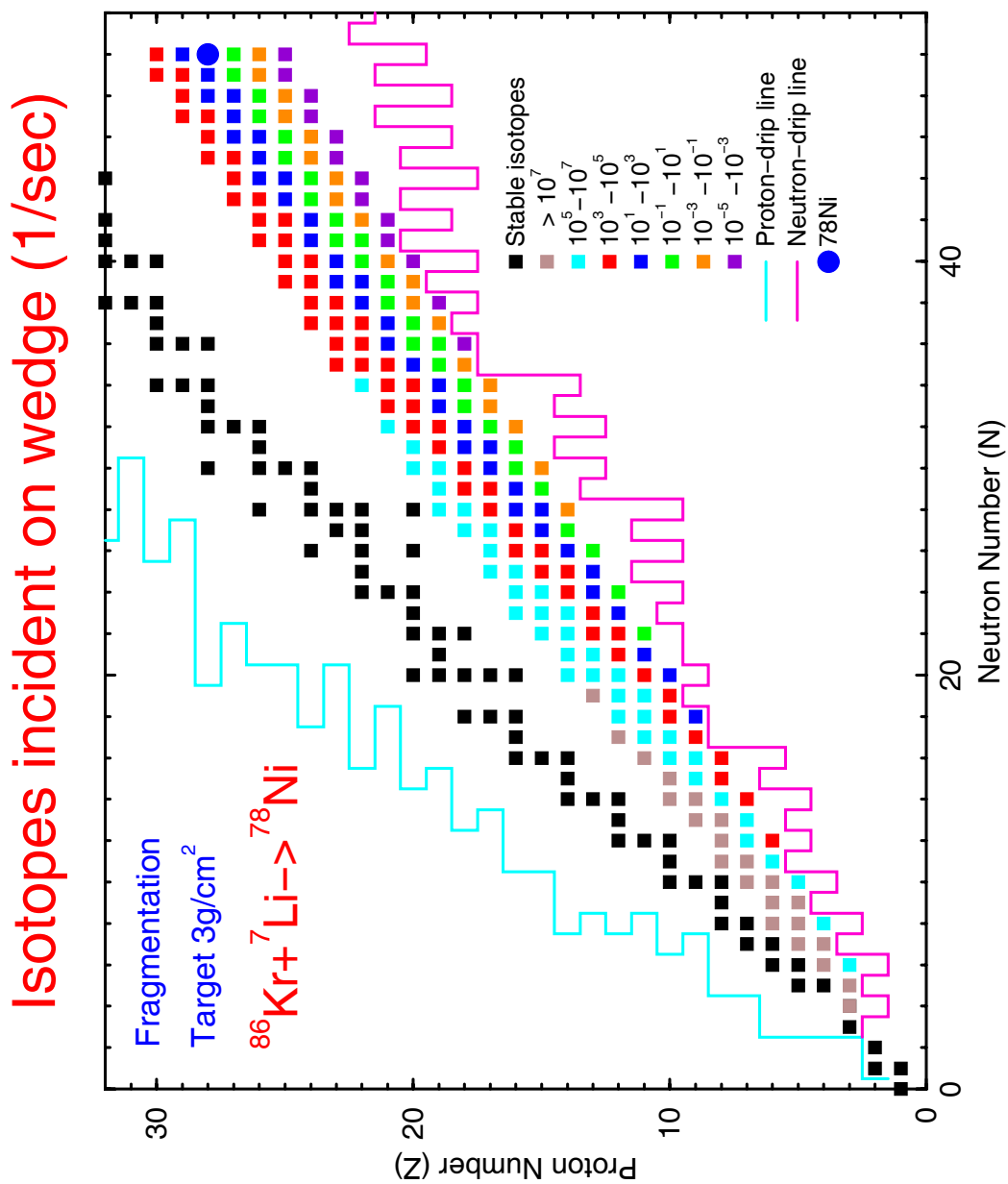
Fig. III-33. *Z-N distribution of contaminants in a ^{78}Ni beam without the use of a wedge in the separator for the case of Fig. III-32.*
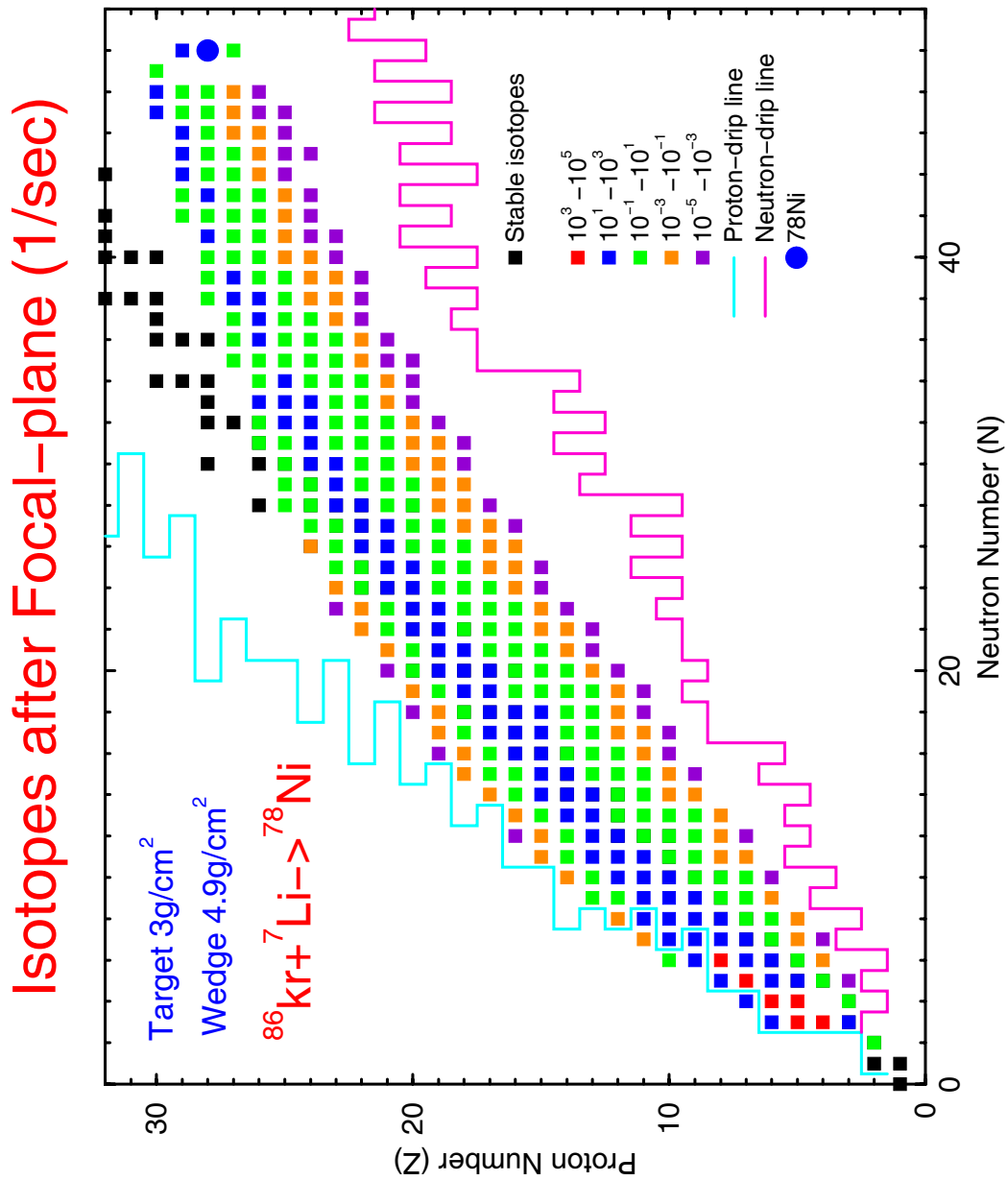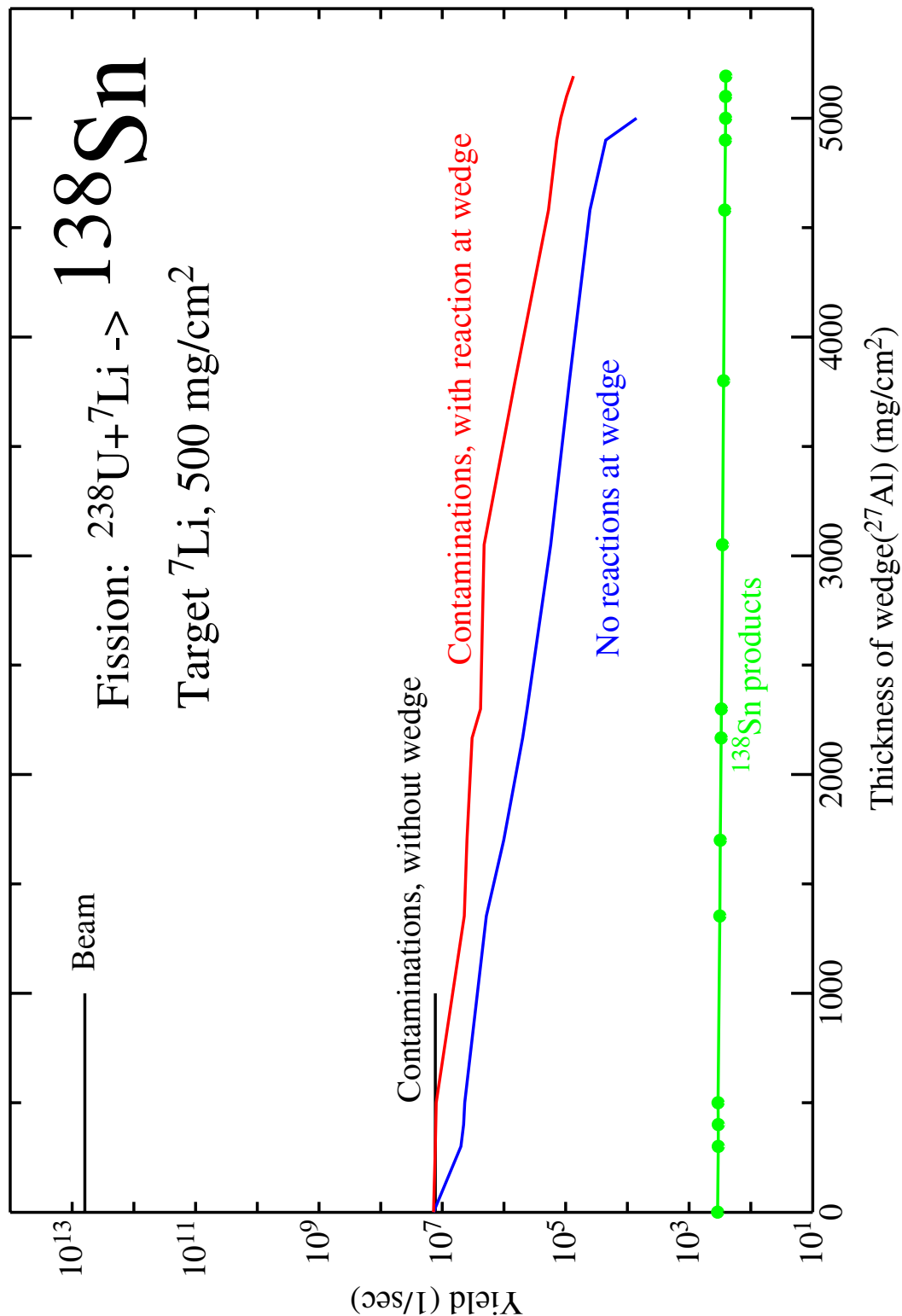
Fig. III-34. *Z-N distribution of contaminants for ^{78}Ni beam with the use of an Al wedge of thickness 4.9 g/cm^2 in the separator for the case of Fig. III-32.*

Fig.III-35. *The beam contaminant yields computed with (solid curve) and without (dashed curve) including reactions in the wedge is compared to the ^{138}Sn yield (dotted curve) produced via in-flight fission of a 400 MeV/u, 100kW ^{238}U primary beam on a 0.5 g/cm^2 ^7Li target as a function of the thickness of the wedge.*

b.5.   Simulation of Effusion from Targets of Tilted Foils (B. Mustapha and J. A. Nolen)

Replacing a target transverse to the beam by a 10 times thinner one tilted at about 6° from the beam direction reduces the thickness for heat transfer and diffusion by a factor of 10 while keeping the same production thickness. This concept makes the target cool faster and therefore supports higher beam power. Monte-Carlo effusion simulations of targets based on this concept were carried out to find optimum target geometries for both fast and slow diffusion materials.

For a foil tilted at about 6° from the beam direction, the foil area, as well as the effective thickness seen by the beam, are about 10 times larger than the configuration where the foil is transverse to the beam direction used in most existing facilities. For the same production thickness, this concept reduces the real foil thickness for better thermal conductivity and increases the dissipation of power by thermal radiation due to the larger area. The power density is down by a factor of 10. Combined with beam manipulation techniques to irradiate larger target area this concept could reduce a significantly high power density to values that could be supported by a variety of target materials. In addition to making the target sustain higher beam power, the concept of tilted foils reduces the delay from the diffusion process leading to a faster ion release while keeping the production of radioisotopes the same. Figure III-36 is a schematic of this concept.
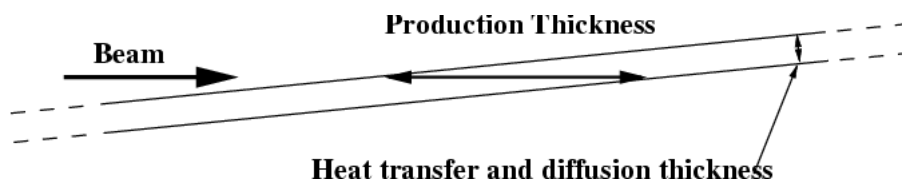

Fig. III-36.   Schematic of tilted-foil target concept.

In earlier simulation studies,[1] we found that for a given geometry the average path length for an effusing particle scales with the total volume of the target and the average number of collisions with the total interior surface. Since the concept of titled foils requires the irradiation of a large target area, the total volume and surface of such targets is significantly larger (i.e. ~ 10 times) than existing ISOL targets which could result in an extra delay in the effusion process. In order to investigate the delay from effusion and optimize the target geometry we performed simulations using Geant-4.[2]

For these simulations we use a 20 cm × 20 cm × 3 mm target foil tilted at 5.7° from the beam direction and placed inside a 21 cm × 21 cm × 3 cm target enclosure. For direct comparison with existing ISOL targets, we use an ISOLDE type ionizer. A 3 mm diameter - 3.5 cm long tungsten tube connected to the target via an 8 mm diameter - 5-cm long tantalum tube. The typical number of events simulated is 10^5. Comparing the average number of collisions and path length to the numbers obtained for the RIST (Radioactive Ion Source Test) target,[3] we notice that even with 10 times the volume of the RIST target, no extra effusion delay is expected for a tilted foil target.

In order to optimize the geometry we studied the dependence of the average number of collisions and path length on the foil thickness and the spacing between the foil and the target enclosure. Figure III-37 shows the results obtained by varying the foil thickness. The point at 0 mm corresponds to the case with no foil and the point at 10 mm correspond to the case where the foil is in contact with the target enclosure. Varying the foil thickness from 1 to 10 mm increased the number of collisions by about 15% due to the increase of the total surface and reduced the path length by about 10% because of the decrease in the volume available for the particles. However, if the sticking time is not negligible, reducing the number of collisions by using a thinner foil could be more favorable.

_____
[1]B. Mustapha and J. A. Nolen, Nucl. Instrum. Meth. **A521**, 59 (2004).
[2]Geant-4 home page at http://geant4.web.cern.ch/geant4/.
[3]B. Mustapha and J.A. Nolen, Nucl. Instr. Meth. **B204**, 286 (2003)
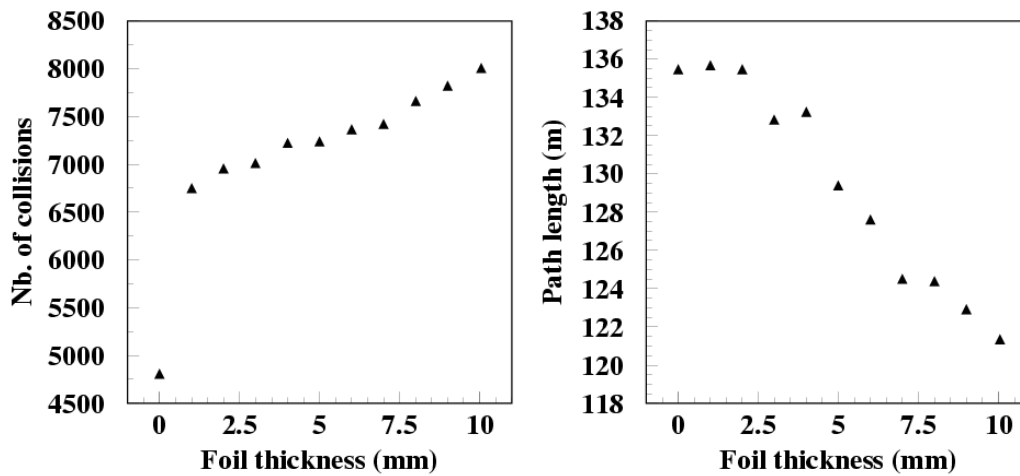
Fig. III-37.   Foil thickness effect on the average number of collisions and path length.

Figure III-38 shows the results obtained by varying the foil-enclosure spacing. Two configurations were used to study this effect: (a) varying the spacing the same way in the 6 directions and (b) varying the spacing only in the direction of the ionizer, in other directions the foil is kept in close contact with the enclosure. We notice that the second configuration (b) is more favorable and that is mainly because the foil divides the total volume into halves communicating only through the ionizer side. For the first configuration (a) we notice a minimum in the number of collisions at about 5 mm spacing and in the path length at about 3 mm spacing. In the case of non-negligible sticking time, the optimum spacing would be the one that minimizes the number of collisions. For the second configuration (b) we notice a kind of plateau for both the number of collisions and path length up to a spacing of 15 mm extra effusion delay is expected for a tilted foil target.
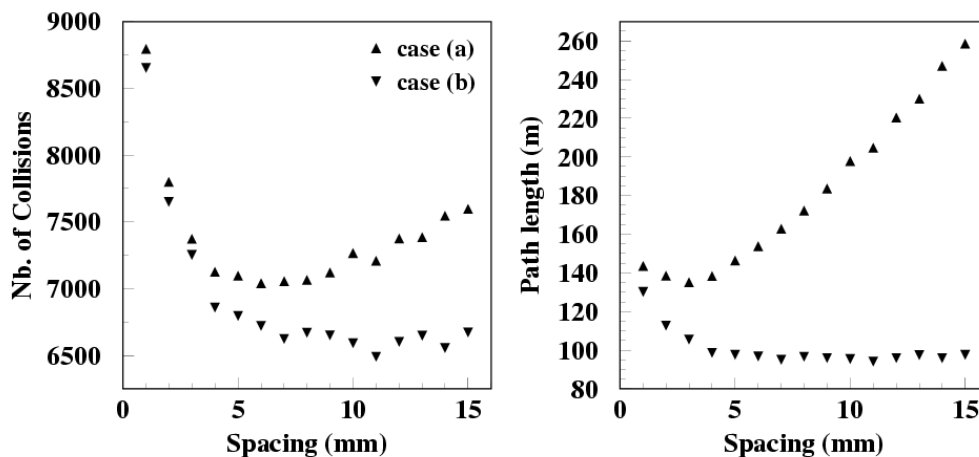

Fig. III-38. Effect of foil-enclosure spacing on the average number of collisions and path length. (a) Case where the spacing is varied in all directions. (b) Case where spacing is varied in the direction of the ionizer only.

In the discussion above, we considered only the effusion part of the release process implicitly assuming fast diffusion from a few mm thick foil. For slower diffusion materials, we may consider sub-dividing the target foil into 10 or more foils. We performed effusion simulations for the case of ten 0.3 mm thick foils making 3 mm total thickness. The effect of the spacing between foils is studied.   Figure III-39 shows the average number of collisions and path length as function of the spacing between foils. A more than 50% decrease in the number of collisions is observed when increasing the spacing from 1 to 2 mm. The path length shows a minimum for 2 mm spacing.
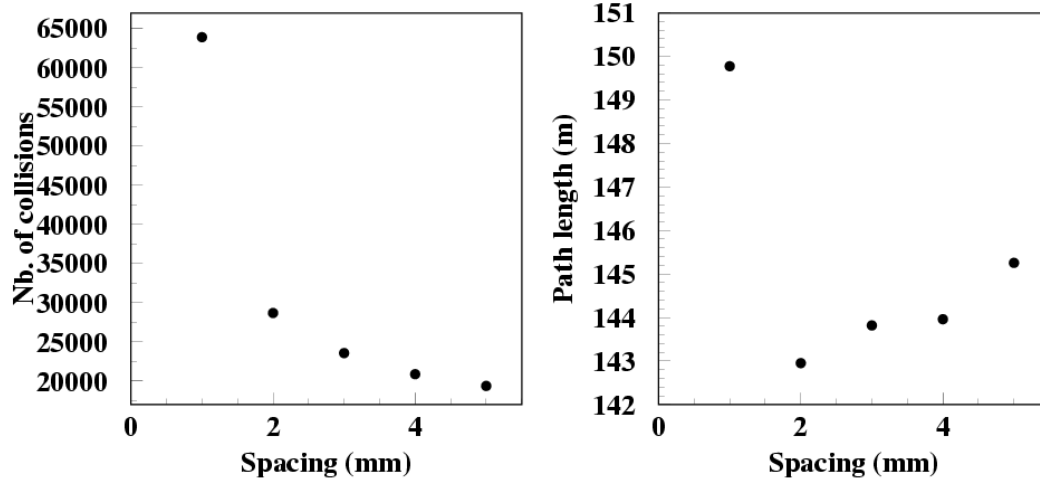

Fig. III-39. Dependence of the average number of collisions and path length on the spacing between foils in the case multiple foils, here 10.